

THE EFFECTS OF EXCESS SODIUM AND SINTERING
PARAMETERS ON IONIC CONDUCTIVITY OF
ZINC STABILIZED β' -ALUMINA

BY

ANASTASIA M. FREDELL

A THESIS
SUBMITTED TO THE FACULTY OF

ALFRED UNIVERSITY

IN PARTIAL FULFILLMENT OF THE REQUIREMENTS
FOR THE DEGREE OF

MASTER OF SCIENCE

IN

CERAMIC ENGINEERING

ALFRED, NEW YORK

APRIL 24, 2015

Alfred University theses are copyright protected and may be used for education or personal research only. Reproduction or distribution in part or whole is prohibited without written permission from the author.

Signature page may be viewed at Scholes Library, New York State College of Ceramics, Alfred University, Alfred, New York.

THE EFFECTS OF EXCESS SODIUM AND SINTERING
PARAMETERS ON IONIC CONDUCTIVITY OF
ZINC STABILIZED β'' -ALUMINA

BY

ANASTASIA M. FREDELL

B.S. ALFRED UNIVERSITY (2013)

SIGNATURE OF AUTHOR _____

APPROVED BY _____

DR. DOREEN EDWARDS, ADVISOR

DR. ALASTAIR CORMACK, ADVISORY COMMITTEE

DR. SCOTT MISTURE, ADVISORY COMMITTEE

CHAIR, ORAL THESIS DEFENSE

ACCEPTED BY _____

DOREEN D. EDWARDS, DEAN
KAZUO INAMORI SCHOOL OF ENGINEERING

ACKNOWLEDGMENTS

First, I would like to thank my thesis advisor, Dr. Doreen Edwards for her support and assistance with this project. Doreen is a phenomenal woman, advisor and Dean; I consider myself very lucky to have been given the opportunity to work in her group. Thank you to my committee members, Dr. Scott Misture and Dr. Alastair Cormack, and project consultants Dr. Bu Wang and Sean Sweeney for their much needed support and guidance throughout this project. Additionally, I would like to thank Brittany Higgins and Gerry Wynick for their extensive help with SEM imaging. Many thanks to Krishna Amin for help coordinating ICP analysis, for always putting a smile on my face, and for providing an endless supply of candy. Thanks to Katie Decker and Tiffany Horton for their assistance with scheduling, ordering, and answering my many questions.

Thanks to Kyle McDevitt for his assistance with late night XRD runs and help with data analysis. To Lucas Holmes for always being available to help me with a variety of miscellaneous tasks, day or night, and generally being the best ‘minion’ anyone could ask for. To my bad ass research group, Claire Dvorak, Mike Alberga and Brittany “DonCheadle” Higgins for lots of much needed advice, a boatload of entertainment and lasting friendships. [#TeamEdwards]. Huge thanks to my family for their support throughout the last 6 years of higher education (undergrad and grad school) and for never failing to remind me that “Girls can do anything!” Lastly, many thanks to Kevin Keefe; not only for delivering the yummiest of lunches and dinners to me during marathon stretches in the office but also for his always abundant love and support throughout every test, challenge and breakthrough that has come with earning both a Bachelor’s and Master’s degree. I am truly blessed to have such wonderful people supporting me.

This work was funded by NYSERDA and GE Global Research under a NY-BEST program at The Center for Advanced Ceramic Technology at Alfred University. NYSERDA has not reviewed the information contained herein, and the opinions expressed in this report do not necessarily reflect those of NYSERDA or the State of New York.

TABLE OF CONTENTS

	Page
Acknowledgments	iii
Table of Contents	iv
List of Tables	vi
List of Figures	viii
Abstract	xi
I. INTRODUCTION.....	1
II. LITERATURE REVIEW.....	3
A. Material Background	3
1. β and β' -Alumina Background	3
2. Applications.....	7
a. Sodium Sulfur Batteries	7
b. ZEBRA Batteries	9
3. Zinc Doped β' Alumina.....	10
4. Processing Na β' -Alumina	11
B. Impedance Spectroscopy Background.....	14
III. EXPERIMENTAL PROCEDURE.....	18
A. Powder Synthesis.....	18
B. Sample Forming	21
C. Sintering of Samples.....	22
1. Sintering Setup.....	22
2. Sintering Parameters.....	23
D. Density Measurements	23
E. SEM.....	24
1. Sample Preparation and Imaging Conditions.....	24
2. Grain Size Analysis	25
F. Impedance Spectroscopy	25
1. Sample Preparation and Equipment Operation	25
2. Data Analysis.....	29
G. XRD.....	34
H. ICP.....	35
IV. RESULTS AND DISCUSSION.....	36
A. Effect of Electrode Material on Impedance Spectroscopy Measurements	36

B.	Excess Soda Studies	45
1.	Composition.....	45
2.	Material Properties.....	47
a.	Density (Effect of Sintering and Composition on Density)	47
b.	Microstructure and Grain Size (Effect of Sintering and Composition on Grain Size)	49
c.	XRD	52
d.	ICP	59
3.	Electrical Properties.....	61
4.	Relationships	64
a.	Effect of Grain Size on Resistivity and Activation Energy.....	64
b.	Effect of Density on Resistivity and Activation Energy	66
V.	SUMMARY AND CONCLUSIONS.....	68
A.	Effect of Electrode Material on Impedance Measurements.....	68
B.	Effect of Composition and Sintering on Electrical Properties.....	69
VI.	FUTURE WORK	71
	REFERENCES.....	72
	APPENDIX.....	76

LIST OF TABLES

	Page
Table I. Relation of Impedance to Equivalent Electrical Circuit Elements	15
Table II. Calcining Procedure for Formation of Zinc Stabilized Na $\beta^{\prime\prime}$ -Alumina Phase with No Organics Remaining.....	20
Table III. SEM Imaging Conditions Used to Obtain Photomicrographs.....	24
Table IV. Sweep Parameters for Closed Circuit Measurement	26
Table V. Fitting Parameters for Equivalent Circuit Data	26
Table VI. Impedance Sweep Parameters Used to Collect Sample Data.....	28
Table VII. Parameters for Diffraction Experiments Performed on Powder and Solid Samples.....	34
Table VIII. XRD Measurement Parameters.....	35
Table IX. Measured Sample Resistivity and Activation Energy for Samples Measured Using Four Different Electrode Materials	44
Table X. Composition Targets for Ideal Zinc Doped Composition ($\text{Na}_{1.67}\text{Zn}_{0.67}\text{Al}_{10.33}\text{O}_{17}$)	45
Table XI. Composition Targets for Z3 Powder (Excess Na/Al = 0.01)	45
Table XII. Composition Targets for Z4 Powder (Excess Na/Al = 0.02)	46
Table XIII. Density of Sintered Pellets Pressed from Composition Z3 Powder	47
Table XIV. Density of Sintered Pellets Pressed from Composition Z4 Powder	48
Table XV. Average Measured Grain Sizes for Sintered Samples	51
Table XVI. Peak Areas of Secondary Phase (NaAlO_2) for all Sintered Samples of Both Compositions	57

Table XVII. ICP Analysis of Zn/Al and Na/Al Molar Ratios in Powders and Samples .. 59

|

LIST OF FIGURES

	Page
Figure 1. Unit cells for (a) β'' and (b) β -alumina.	4
Figure 2. A section of the $\text{Na}_2\text{O-MgO-Al}_2\text{O}_3$ phase diagram. ²⁷	6
Figure 3. NAS battery cell: principle of operation.	8
Figure 4. Schematic of a typical NAS cell.....	9
Figure 5. Ideal Nyquist plot showing contribution of grains, grain boundaries and electrode.....	16
Figure 6. Flow chart depicting the processing route used to make zinc doped $\text{Na } \beta''$ -alumina used in this research.	18
Figure 7. Quick sweep impedance data illustrating poor sample connection.....	27
Figure 8. Quick sweep impedance data illustrating good sample connection.	27
Figure 9. Examples of raw uncompensated and compensated impedance data.	28
Figure 10. Representative impedance spectra for sintered samples.	29
Figure 11. The effect of the number of data points used determined resistance.	30
Figure 12. Sample Excel spreadsheet used to organize raw data and determine sample resistance at a given temperature.	31
Figure 13. Sample of condensed electrical data for one sample over the desired temperature range.....	32
Figure 14. Resistivity vs. thickness for samples of different thicknesses measured using four different electrode materials at 300 °C. Linear trend lines were fit to the data with varying success (see text).....	36
Figure 15. Example of the graph used to determine the contact resistance for samples over a range of temperatures.....	38

Figure 16. Contact resistance as a function of temperature measured using four different electrode materials.	39
Figure 17. Sample resistance with respect to thickness for samples measured with different electrode materials. Data has been corrected to exclude contact resistance. Linear trend lines were fit to the data with varying success (see text).	40
Figure 18. Resistivity vs. sample thickness at 300 °C for samples measured using four different electrode materials. (Corrected to account for contact resistance). .	42
Figure 19. Resistivity vs. sample thickness at 300 °C for four different electrode materials used to measure the same samples.....	43
Figure 20. Activation energy vs. sample thickness for different electrode materials used to measure the same sample sets.....	44
Figure 21. Spray dried granules for Z3 and Z4 compositions.	46
Figure 22. Effect of sintering temperature on percent theoretical density of sintered samples.....	48
Figure 23. Photomicrographs Show Samples of Z3 and Z4 Compositions Sintered to Different Conditions Producing Different Average Grain Sizes.	50
Figure 24. Effect of sintering time, temperature and composition on average grain size.	51
Figure 25. XRD pattern for a sintered sample of zinc doped β'' -alumina identified and matched with corresponding XRD cards for the primary phase.....	53
Figure 26. XRD pattern of sintered zinc doped β'' -alumina. The primary phase is identified as well as the minor secondary phase (NaAlO_2).	54
Figure 27. XRD patterns for composition Z3 samples comparing the relative size of the two main peaks for the secondary phase (NaAlO_2) between sintering conditions.....	55
Figure 28. XRD patterns for composition Z4 samples comparing the relative size of the two main peaks for the secondary phase (NaAlO_2) between sintering conditions.....	56
Figure 29. Peak area for the two main sodium aluminate peaks (roughly 30 and 33 °2 θ).	57

Figure 30. Calculation of crystallite size for $30^\circ 2\theta$ and $33^\circ 2\theta$ using peak fitting and the Scherrer Equation.....	58
Figure 31. Effect of sintering time and temperature on Zn/Al and Na/Al ratios.	59
Figure 32. Arrhenius plots for sintered samples of both Z3 and Z4 compositions over a variety of sintering temperatures and sintering times.	61
Figure 33. Resistivity vs. temperature for a variety of sintered samples of composition Z3 (0.01 Na/Al excess).....	62
Figure 34. Resistivity vs. temperature for a variety of sintered samples of composition Z4 (0.02 Na/Al excess).....	63
Figure 35. Resistivity vs. grain size for sintered samples.....	64
Figure 36. Activation energy vs. grain size for sintered samples.	65
Figure 37. Resistivity vs. density for sintered samples.....	66
Figure 38. Activation Energy vs. density for sintered samples.	67
Figure 39. Batch sheet for Z3 composition.....	76
Figure 40. Batch sheet for Z4 composition.....	77
Figure 41. TGA data for uncalcined powder of Z3 composition.....	78

ABSTRACT

Sodium β'' -alumina is used in batteries due to its high ionic conductivity. This work studied the effect of excess sodium on the grain size, sintering behavior, and ionic conductivity of zinc stabilized β'' -alumina. Two compositions, each with varying amounts of excess sodium (molar Na/Al = 0.01 & 0.02), were synthesized and sintered at varying temperatures and times (1610 °C, 1625 °C and 1640 °C; 30 minutes and 1 hour). It was found that grain size and density had the largest influence on ionic resistivity in the materials and that the presence of increased sodium in the composition did not aid in sintering or decrease ionic resistivity.

Which factors affect AC impedance spectroscopy, used to measure ionic conductivity in these materials, is not fully understood. The effects of sample thickness and electrode material were evaluated to determine the repeatability of data across these parameters. A connection between these factors was established. Resistivity was determined to be independent of sample thickness; although thinner samples exhibited greater uncertainty in collected data. Additionally, it was determined that of the choice of electrode material did influence collected data. Resistivity and activation energy for samples measured using gold and fluxed platinum electrode could be directly compared to each other, whereas the data collected using unfluxed platinum and carbon electrodes could not; showing that electrode material did affect impedance spectroscopy measurements.

I. INTRODUCTION

In the last fifty years, sodium β -alumina materials have been investigated for a variety of applications. Primarily, research has focused on the use of these materials in batteries, as a solid electrolyte. The development and improvement of energy related technologies has become increasingly more important as the global demand for energy has continued to rise. The demand for better performing batteries has become particularly important as remote and distributed energy applications become more abundant. Remote data storage facilities, battery powered/hybrid vehicles, and alternative energy applications like windmills have all made the need for reliable, high performing batteries that much greater.

The development of battery technology has driven the development and research of the materials used in these batteries, because even slight improvements in individual components of the battery translate into increased efficiency of the system overall. In 1967 it was quickly realized that β -alumina had extreme potential in what, at that time was a highly explosive period of battery research. Work with β -alumina soon led to the discovery of β'' -alumina; a better performing variation of the material.¹ The discovery of β'' -alumina helped improve battery functionality and further fueled research into its synthesis and uses. The β'' -alumina structure requires stabilization by a dopant cation to remain in a stable phase. Extensive research into stabilization through the introduction of Li^+ and Mg^{2+} ions has been performed.²⁻⁵ Stabilization using other cations, both monovalent and divalent has been investigated.⁶⁻¹² In this work, zinc cations (Zn^{2+}) were used to stabilize the β'' -alumina structure.

The β'' -alumina structure features broad sodium conduction planes that make the transport of sodium ions through the material very efficient.^{13, 14} However, the presence of sodium presents a problem when processing is considered. Sodium volatility at high temperatures means that soda loss in these systems presents a real challenge to producing a final composition with the desired amount of sodium. Therefore, excess soda is often used in processing to counteract the effects of soda loss during synthesis.¹⁵ However, including the correct amount of excess soda for processing without introducing too much

soda into the system is very difficult. Often times, synthesizing β'' -alumina with the correct stoichiometric amount of sodium does not occur, and small amounts of excess soda can be present in the final composition. One objective of this work was to evaluate the effects of small amounts of excess soda on properties of the final product including density, grain size and ionic resistivity.

The evaluation of ionic transport properties of some materials can be difficult in practice. AC impedance spectroscopy has been widely used to evaluate electrical properties of ionic conductors, but the number of factors can influence the data and their effects are not always well understood. In particular it has been hypothesized that the type of electrode material used in sample testing, as well as variations in sample thickness can affect the final experimental results. Understanding how these factors affect data and whether data collected in one location using one method can be compared to data obtained from another source, possibly using other electrode materials, needs to be better understood. Further understanding of how changes in sample thickness and electrode materials affect experimental results will allow scientists to better compare global data. Therefore, the second portion of this research will focus on variations in impedance measurements, specifically the effect of electrode material and sample thickness on experimental results.

II. LITERATURE REVIEW

A. Material Background

1. β and β'' -Alumina Background

Although β -alumina was first synthesized as a byproduct of the Bayer process in the late 1800s, its structure was not characterized until the 1930s when Bragg used X-ray diffraction to determine its structure.¹³ Early on, the material was used for refractories and was not of particular interest to scientists until about 30 year later, when researchers at Ford Motor Company began investigating the properties of the material further. Yao and Kummer published two papers in 1967 detailing the effects of the material's structure on what they reported to be an extraordinarily high ionic conductivity of the material, and its potential use as a solid electrolyte.¹ This sparked an enormous amount of research worldwide at a time where alternate energy sources were a booming area of research, in hopes that they would lighten the world's dependence on fossil fuels. These initial works spurred half a century of research into β -aluminas, specifically for battery applications that still continues today.

The group of materials commonly referred to as β -alumina is comprised of aluminum oxide materials that exhibit loosely packed layers between close packed slabs. The loosely packed layers are comprised of mobile sodium (Na^+) and stationary oxygen (O^{2-}) ions and are commonly referred to as 'conduction planes.' The closely packed slabs contain both oxygen (O^{2-}) and aluminum ions (Al^{3+}) in octahedral and tetrahedral coordination, which form defect spinel-like blocks that are bonded together by the conduction planes. There are two main crystal structures in the β -alumina family; β and β'' . β -alumina ($\text{Na}_{1+x}\text{Al}_{11}\text{O}_{17+x/2}$; $0.15 \leq x \leq 0.3$) has a hexagonal symmetry ($a=0.559$ nm, $c=2.261$ nm) with space group $\text{P6}_3/\text{mmc}$ and has a unit cell composed of a conduction plane sandwiched between two spinel blocks^{13, 14, 16}. β'' -alumina ($\text{Na}_{1+z}\text{Mg}_z\text{Al}_{11-z}\text{O}_{17}$; $0.5 \leq z \leq 1$) on the other hand has a rhombohedral symmetry ($a=0.56$ nm, $c=3.395$ nm) with space group $\text{R}\bar{3}\text{m}$ and contains two conduction planes separated by three spinel

blocks¹⁷⁻¹⁹. As a result, β'' has a higher concentration of sodium per formula unit. The unit cells of each material are shown in Figure 1.¹⁶

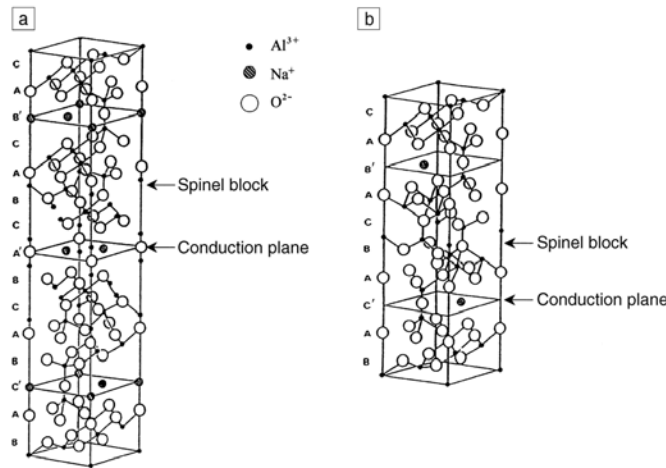


Figure 1. Unit cells for (a) β'' and (b) β -alumina.

The differences in stacking between the two materials cause the unit cell of β'' -alumina to be roughly 50% larger than that of the β -alumina unit cell. Additionally, the two materials have different ionic arrangements in the conduction planes. β -alumina has sodium ions and bridging oxygen ions that are localized on a mirror plane at $z=1/4$ and $z=3/4$, and a conduction plane thickness of roughly 2 \AA ^{16, 20}. As a result, sodium ions move relatively freely inside the conduction plane, but larger ions are far less mobile. This is not the case with β'' -alumina where no mirror plane exists in the structure. In the β'' phase, spinel blocks are rotated 120° with respect to one another; sodium and oxygen ions in the conduction plane are slightly displaced from one another in the c -direction. This causes the thickness of the conduction plane of β'' -alumina to be larger than that of β -alumina, roughly 3 \AA . The increased thickness results in the ability for ions larger than sodium to be mobile within the conduction plane: a phenomenon that has been explored further in ion-exchange studies.^{1, 21, 22} In both β and β'' structures, ion mobility inside conduction planes is two dimensional. Conduction is very high in the planes perpendicular to the c -direction and essentially zero in the plane parallel to the c -direction.¹⁶

Although there are many similarities between the two materials, the subtle differences in structure and stoichiometry are enough to affect their respective

mechanical and electrical performances. The ideal stoichiometric formula for β -alumina materials is $(\text{Na}_2\text{O})_{1+x}\text{Al}_2\text{O}_3$ where $x=0$; however, both β and β'' -alumina usually contain excess sodium in their structures.^{16, 19, 23} The formula most commonly associated with the β -alumina phase is $\text{Na}_{1+x}\text{Al}_{11}\text{O}_{17+x/2}$ where x ranges from 0.15 to 0.3.¹⁶ Excess sodium ions in the β -alumina structure are compensated by oxygen ions on interstitial sites in the conduction plane. The stoichiometry of β'' is slightly more complicated.

On its own, β'' -alumina is metastable and tends to decompose into β -alumina if the structure is not stabilized.²⁴ To stabilize the structure, monovalent or divalent cations must be used to replace an aluminum ion (Al^{3+}) in the spinel block.¹⁷ This helps suppress the crystalline transition of β'' to β -alumina. Specifically, the substitution takes place utilizing an aluminum ion located on a tetrahedral site near the center of the spinel block; position Al(2).²⁵ Once this substitution is completed, the binary $\text{Na}_2\text{O}-\text{Al}_2\text{O}_3$ system becomes a ternary $\text{Na}_2\text{O}-\text{MO}/\text{M}_2\text{O}-\text{Al}_2\text{O}_3$ system where M is the element used to stabilize the system.¹⁵ The substitution results in a charge imbalance; to maintain charge neutrality, more sodium ions are incorporated into the structure. In this way, each individual aluminum ion substitution is charge balanced with the insertion of a sodium ion into the conduction plane and the cation onto the aluminum site. Stabilization of the β'' -alumina structure allows for higher levels of sodium accommodations, further improving the ionic conductivity of the material.

It should be noted that deviations in structure between the two phases also causes a difference in the mechanisms by which ionic conductivity occurs. The introduction of the extra sodium ion in the structure as a means of charge balancing the stabilization substitution ($\text{Al}^{3+} \leftrightarrow \text{M}^{2+} + \text{Na}^+$) impacts the number of sodium vacancies in the structure. In unstabilized β'' -alumina, there are three unoccupied sodium sites in the unit cell, one at each of the three conduction planes. When stabilization occurs, vacant sites become occupied by the introduction of sodium ions for each corresponding spinel block. In practice, not all sodium vacancies are removed upon stabilization, and these remaining vacancies contribute to the ionic conductivity of the material. As a result, the mechanism by which ionic conduction occurs in the stabilized β'' -alumina structure is best described as a vacancy mechanism, although not in its purest sense. The mechanism for β -alumina is somewhat different due to the excess sodium ions commonly found as interstitial sites

in the conduction planes of the material. This excess sodium causes an interstitial mechanism of ion conduction in the material; different from that of the β'' -alumina phase. As a result, the ionic conductivity of stabilized β'' -alumina is greater than that of β -alumina.

Stabilized β'' -alumina has been extensively researched; most abundantly the structures that have been stabilized using monovalent lithium (Li^+) and divalent magnesium (Mg^{2+}). These two cations appear in a multitude of studies as stabilizing species, independently as well as in tandem.^{2-4, 26} For magnesium doped materials, the stoichiometry is as follows, $\text{Na}_{1+z}\text{Mg}_z\text{Al}_{11-z}\text{O}_{17}$ where $0.5 \leq z \leq 1$.¹⁹ The ideal composition occurs when $z=0.67$ yielding the chemical structure $\text{Na}_{1.67}\text{Mg}_{0.67}\text{Al}_{10.33}\text{O}_{17}$.²³ Lithium stabilization follows $\text{Na}_{2-z}\text{Li}_z\text{Al}_{11-z}\text{O}_{17}$ where $0.0 \leq z \leq 0.5$, with ideal composition of $\text{Na}_{1.67}\text{Li}_{0.33}\text{Al}_{10.67}\text{O}_{17}$. A portion of the Na_2O - MgO - Al_2O_3 phase diagram is shown in Figure 2.

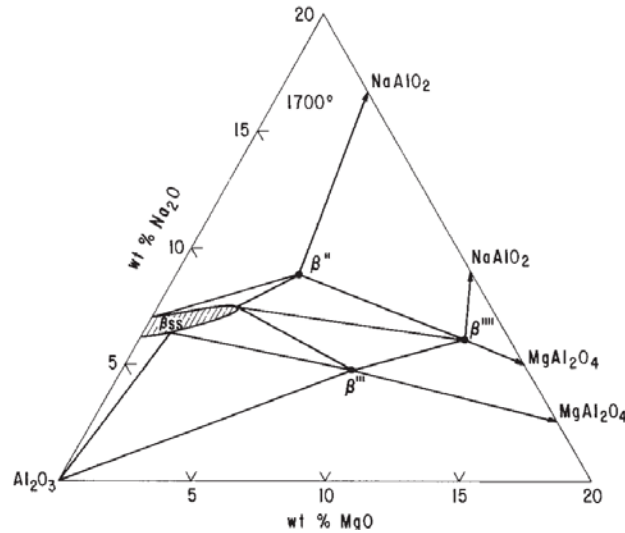


Figure 2. A section of the Na_2O - MgO - Al_2O_3 phase diagram.²⁷

This phase diagram created by Weber and Venero shows detailed phase equilibria in the ternary stabilized system.²⁷ The presence of two additional phases β''' and β'''' are indicated. However, these phases are somewhat unimportant as they cannot remain in thermodynamic equilibrium with Al_2O_3 .⁶ This phase diagram highlights the location of the β'' -alumina phase field with regards to oxide composition. Additionally it should be noted that although a body of research exists focusing on the adaptation of β -alumina

structures through ion exchange with sodium ions in the conduction plane, it is not addressed in this work. For the entirety of this work, the terms β -alumina and β'' -alumina refer to structures containing only sodium as mobile ions in the conduction planes.

2. Applications

The two forms of beta alumina, β and β'' -alumina have been studied extensively throughout the past 50 years. Although there have been several applications, the overwhelming use of the material has been as a solid electrolyte material in batteries. The development of two battery types in particular have driven research of β'' -alumina solid electrolytes; NAS (sodium sulfur) and ZEBRA (nickel chloride) batteries.^{1, 5, 23, 28-32} β'' -alumina is incredibly useful as a solid electrolyte material in batteries due to its fast ion-conducting nature. In these batteries, sodium ions are transferred from anode to cathodes to charge and discharge the cell. Therefore the optimization of sodium conduction through the solid electrolyte material has been heavily researched as a means to optimize the overall efficiency of these batteries.

a. Sodium Sulfur Batteries

The use of β'' -alumina as a solid electrolyte material was first proposed by Kummer and Yao in 1967.¹ Sodium sulfur batteries, often referred to as NAS batteries, use sodium and sulfur as the active electrode materials. Sodium acts as the negative electrode and sulfur acts as the positive electrode. The two electrodes are physically separated using a β'' -alumina solid electrolyte. NAS batteries are preferred over conventional lead-acid batteries due to their much higher energy density.^{23, 28} The energy density of a conventional lead-acid battery ranges from 41 to 48 W•h/kg while the energy density of NAS batteries is roughly 100-150 W•h/kg. Additionally, NAS batteries have high life cycles; usually 4500 cycles to 90% and 40,000+ cycles to 20%.²⁹ One drawback to NAS batteries is the temperature of operation. NAS batteries operate at a temperature of roughly 300-350 °C to keep the active electrode material molten during operation.⁵ Although this does help reduce the sodium ion transfer resistance through the β'' -

alumina electrolyte, it also means that the battery must be well insulated. Figure 3 shows the principle of operation for the NAS battery cell.²⁹

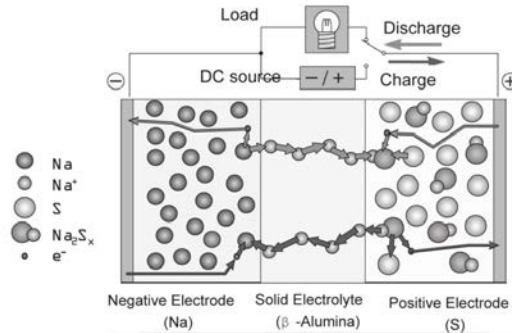
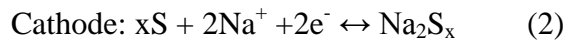
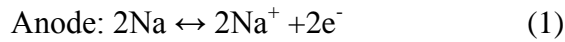


Figure 3. NAS battery cell: principle of operation.

It is observed that during charging and discharging, a reversible electrochemical reaction takes place. During discharging, sodium at the negative electrode releases electrons to the circuit and the resulting sodium ions are then passed through the β'' -alumina solid electrolyte. When these ions reach the other side of the ceramic, they come into contact with the sulfur and form sodium polysulfide (Na_2S_x). After full discharge, the process is reversed for charging of the cell. Decomposition of the sodium polysulfide phase occurs and sodium ions travel back across the ceramic separator to the negative electrode. This constitutes one charge/discharge cycle for the cell. The amount and phase of sodium polysulfide varies as the discharging and charging processes occur.^{1, 5} The anode and cathode reaction equations are shown in Equations 1 and 2.²⁸



The geometry of NAS batteries is most often cylindrical. It is observed that the sodium negative electrode sits in the center of the cell, acting as the core. The positive sulfur electrode resides on the outside of the cell and the two electrode materials are separated by a β'' -alumina tube, closed at one end. Figure 4 shows a schematic of a typical cell.²⁹

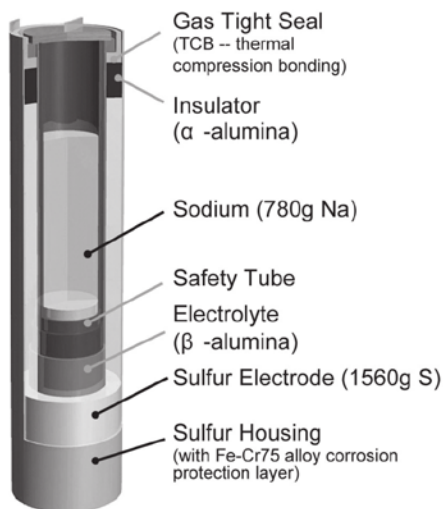
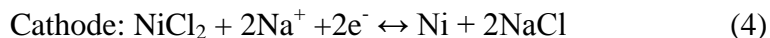


Figure 4. Schematic of a typical NAS cell.

The reason for the cylindrical shape of the cell is due to the mechanical performance of β'' -alumina. This tube geometry provides better stability as opposed to a plate/wall type separator. This allows for maximum strength of the solid electrolyte, which is important: if the ceramic fails and the electrodes come in contact with one another, the battery shorts out.²⁹ The cylindrical shape also helps with energy density optimization of the battery due to the larger volume of sulfur necessary for functionality.

b. ZEBRA Batteries

Developed in the 1980s, ZEBRA batteries are made of sodium and metal chloride electrodes. The sodium, which is typically molten, acts as the negative electrode. The metal chloride, usually a form of nickel chloride (NiCl_2) is the positive electrode.³² The addition of molten NaAlCl_4 in the positive electrode volume allows for the rapid transport of sodium ions between the solid electrolyte material and the solid nickel chloride that acts at the primary positive electrode. The mechanism for the operation of these batteries is similar to those of NAS batteries. First, electrons are given to the cell and sodium ions at the negative electrode move through the β'' -alumina solid electrolyte to reach the positive electrode. When the sodium ions come into contact with the nickel chloride, they form 2 molecules of NaCl salt and precipitate solid nickel.^{5, 32} The anode and cathode reaction equations are shown in Equations 3 and 4.²⁸



When charged, the reaction is reversed. The design of ZEBRA batteries is very similar to those of NAS batteries, where a cylindrical cell is utilized. However, in these batteries the positive electrolyte mix is placed at the core while sodium is held near the walls of the cell. As in NAS batteries, the β'' -alumina material is used to separate the two materials. ZEBRA batteries are designed mostly for automotive applications, usually in vans and buses. ZEBRA batteries are considered to be safer than NAS batteries because the majority of the electrode materials are solid. The energy density of ZEBRA batteries is in excess of 150 W•h/kg.³³

3. Zinc Doped β'' Alumina

Stabilization of β'' -alumina through the use of lithium (Li^+) and magnesium (Mg^{2+}) ions is pervasive in literature as well as in practice. These two cations work well to stabilize the structure of the material and promote increased conductivity. However, their domination as stabilizing ions does not mean that they are the only cations that can be used to produce stable phases of Na β'' -alumina. In fact, many other cationic species (mostly divalent) have been used to successfully stabilize the material. Separate research by Hodge and Kennedy utilized divalent cations of calcium and iron respectively to stabilize the β'' structure.^{18,24} Work by Boilot and Théry showed that divalent cations with ionic radii smaller than 0.097 nm could all be used to stabilize β'' -alumina.⁸ This has been validated by numerous additional works in which ions of nickel (Ni^{2+}), titanium (Ti^{2+}), cobalt (Co^{2+}) and zinc (Zn^{2+}) have all been used to stabilize the β'' structure as well.⁹⁻¹²

It has been observed that the substitution of Zn^{2+} on the Al(2) site in the β'' -alumina structure results in an expansion of the M-O tetrahedral bond length by roughly 8%. It was shown that this expansion did not have any significant effect on the stability of the lattice as a whole, the structure of the conduction planes within the material or the ionic conductivity of ions within this plane.³⁵ However, it has been observed that the conductivity for samples stabilized using ZnO sources is slightly lower than samples that

had been stabilized through the introduction of lithium (Li^+).³⁶ This same study noted the presence of zinc ions in the conduction planes of the material from excess ZnO precursor used in synthesis, insinuating that these ions are responsible for the lower conductivity of the phase.³⁷ This notion is supported by work linking conductivity of β'' -alumina primarily to the composition of the conduction plane, and placing little to no effect on the species of stabilizing ions specifically.¹⁹ Therefore, it can be concluded that correct calculation and addition of divalent precursors is required to stabilize the structure without substituting ions into the conduction plane, which may have negative effects on conductivity. Additionally, it has been observed that the slopes for Arrhenius plots obtained for materials stabilized with zinc ions are largely linear in two regions, with a high temperature activation energy occurring at temperatures above 250 °C and a low temperature activation energy for materials measured below that temperature.^{32,33} A correlation between higher temperature activation energy and ZnO content was also observed; activation energy decreased as ZnO content increased. Lastly, it was observed that zinc stabilization had no effect on grain boundary conductivity.

The use of zinc ions to stabilize Na β'' -alumina is documented in literature as an effective alternative to the conventional stabilization using divalent Mg ions.^{10, 36, 37, 39-41} However, it is important to note that, overall, the effects of sample sintering and microstructure have an overarching effect on sample conductivity; samples need to be sintered to near full density regardless of stabilizing species.⁷ Therefore, consideration of the role of stabilizing species on sintering and densification in the final material is imperative. Magnesium has been reported as an effective sintering and densification aid in β'' -alumina; due to the relatively close ionic radii of Zn^{2+} and Mg^{2+} and their identical substitution methods, it is likely that zinc will also aid in densification and controlled grain growth of the final sintered sample.

4. Processing Na β'' -Alumina

A variety of processing techniques have been researched for the synthesis of β'' -alumina materials. Although most commonly produced using solid state reaction, the use of sol-gel processes, co-precipitation, freeze drying, and deposition have also been investigated.^{24, 42-45} Solid state reaction synthesis is usually achieved by the iteration of

several milling and calcining steps. Disadvantages of solid state synthesis include the potential for soda loss during calcination and the formation of NaAlO_2 at grain boundaries which can increase the susceptibility of the material to degradation by hydration.^{28, 46} Maximizing the final amount of β'' -alumina in the system is most important to final electrical properties, and therefore a number of measures have been tested to this affect, including post-sintering annealing, twin firing schedules, solution based synthesis and even the seeding of pre-calcined materials with preformed β'' -alumina. These processes have all been found to require high degrees of purity in alumina sources and have not garnered optimal results.²⁸

It has been observed that there is a significant effect of precursor alumina type on the formation of β'' -alumina. It has been demonstrated that synthesizing β'' -alumina structures from alpha (α)-alumina precursors results in a mixture between β and β'' phases in the final material as well as bimodal grain sizes, which is not optimal for electrical performance.¹⁶ However, Duncan et al. showed that the use of gamma (γ)-alumina as a precursor provides a structure which lends itself very well to the synthesis of β'' -alumina.⁴⁷ The use of γ -alumina in conjunction with solid state synthesis has been tremendously successful, linked to nearly pure β'' -alumina in the final product from materials reacted at temperatures as low as 1250 °C.⁴⁷ Sintered samples of β'' -alumina synthesized using γ -alumina were observed to have little or no NaAlO_2 or β -alumina side-products present.³⁰ Boehmite ($\text{AlO}(\text{OH})$), a hydrated aluminum oxide) can be used as a starting material prior to powder synthesis. When heat treated to roughly 800 °C it forms γ -alumina, where a cubic closed packed oxygen array is present. During the formation of the β'' -alumina, oxygen ions from the sodium precursor and stabilizing precursor insert themselves between the close packed structure of the gamma alumina. This provides bridging oxygen ions in the structure, and imparts a negative charge. Next, positively charged stabilizing ions insert themselves into the defect spinel blocks. The stabilizing ion effectively pins the structure of the cubic-closed packed oxygen spinel blocks and does not allow sodium ions to diffuse into the spinel structure. This results in the collection of sodium ions in the conduction planes.²⁸ This mechanism allows for the synthesis of β'' -alumina materials at much lower temperatures than synthesis utilizing α -alumina, and aids in the reduction of sodium loss from the system. Additionally, grain

boundary energy is reduced when using γ -alumina, resulting in much less grain growth, which results in consistent fine grain microstructures.⁴⁷

Another important aspect of β'' -alumina synthesis is sodium loss. Sodium volatility at high temperatures causes sodium ions present in the conduction planes to escape from the structure. Although the use of γ -alumina helps decrease synthesis temperatures, aiding in sodium retention, other methods are also utilized to mitigate sodium loss. Commonly, excess sodium is added to the initial batch to account for soda which will be inevitably lost during processing. Therefore, the desired composition can be achieved post synthesis and sintering. However, this inclusion of excess soda must be carefully calculated to prevent NaAlO_2 formation at the grain boundary.¹⁹ Another technique used to combat soda loss involves calcining and sintering samples in closed containers that create sodium rich environments. Often platinum and MgO crucibles are used.^{28, 37, 45} Perfectly counteracting sodium loss using these methods is very difficult to achieve in practice, resulting sometimes in final compositions where excess soda is present.

Once pre-calcined β'' -alumina materials have been synthesized through solid state reaction, final powders are formed. The formation of solid electrolyte materials utilized in batteries can be achieved using a variety of forming techniques; pressing, slip casting and extrusion.¹⁶ The use of isostatic pressing is commonly used and fairly straightforward; however, it requires powders with good flow and die fill, especially in cases where complex electrode geometries are used. To achieve powders with such qualities, spray drying is often used. The use of spray drying allows for the addition of polymers into the ceramic system that aid with green strength and make compact handling more robust. Spray drying also allows for the production of powders that flow easily and exhibit good die fill properties.

B. Impedance Spectroscopy Background

$$V = IR = IZ \quad (5)$$

V = Voltage (volts)

I = Current (Amps)

R = Resistance (Ohms)

Z = Impedance (Ohms)

Ohm's Law (Equation 5) is most commonly used to define resistance; a property which quantifies the opposition of a material to an electrical current. However, this resistance to current flow through a material can also be quantified in terms of impedance. Both resistance and impedance express the opposition to current flow through a material at a given voltage, but there is a notable difference between the two terms.^{48, 49} Mainly, impedance is a complex value that contains both a magnitude and phase component in comparison to resistance, which is only comprised of a magnitude with no phase contribution. Utilizing impedance in electrical testing allows for the evaluation of more complex systems, particularly those which are frequency dependent.⁴⁸⁻⁵⁰

Impedance Spectroscopy (IS) allows for the characterizing of chemical processes through the measurement of electrical properties. This is particularly useful for quantifying ionic conductivity through electrolyte materials, such as β'' -alumina. Impedance spectroscopy measures the current in a material as a function of an applied alternating (AC) current, and compares the amplitude and phase of each signal.^{49, 50} First, a small amplitude AC potential is applied across a sample through two electrodes of a fixed area. The potential fluctuates at a specific range of frequencies and alters the current measured through the sample. Normally the response of the current to the applied voltage is observed as a lag between the two waves, where current lags voltage. This lag is quantified as the phase angle, ϕ . The complex relationship between the applied voltage pulse and the measured current is compiled by the IS analyzer (Solartron) and related to the frequency dependence of impedance using Equation 6.⁴⁹

$$Z(\omega) = \left(\frac{V}{I} \right) = Z_0 e^{j\phi} \quad \therefore \quad Z_o = \left(\frac{V}{I} \right) e^{-j\phi} \quad (6)$$

Z = Impedance (Ohms)

ω = Radial frequency (proportional to $2\pi f$)

V = Applied Voltage (Volts)

I = Measured Current (Amps)

ϕ = Phase Angle (radians)

j = Imaginary component of impedance

As discussed, impedance allows for the quantification of complex electrical behavior through the use of complex numbers. Once obtained, impedance data is commonly fit to an equivalent circuit using electrical elements such as resistors, capacitors and inductors. Impedance correlations for each type of electrical elements are shown in Table I.^{48, 49}

Table I. Relation of Impedance to Equivalent Electrical Circuit Elements

Electrical Element	Corresponding Impedance
Resistor	$Z = R$
Capacitor	$Z = j\omega L$
Inductor	$Z = 1/j\omega C$

Typically, dielectric ceramic materials are modeled using an equivalent circuit of a resistor and capacitor aligned in parallel.^{48, 50} These corresponding impedances are used to calculate the impedance of the equivalent circuit, and express it in terms of real and imaginary components. The real and imaginary components of impedance are plotted on a Nyquist plot, in terms of Z' vs. Z'' . Z' represents the real components of the impedance measurement and Z'' represents the imaginary components or reactants. Nyquist plots are the most common way to represent impedance data.

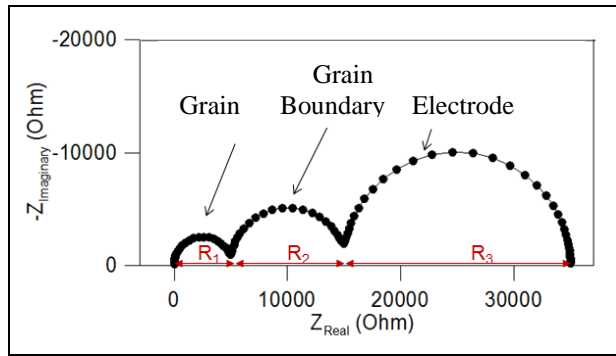


Figure 5. Ideal Nyquist plot showing contribution of grains, grain boundaries and electrode.

Figure 5 shows an ideal Nyquist plot with the contributions of the grain, grain boundary and electrode on the reported impedance data for a ceramic material. In favorable situations, it is possible to separate the effects of the sample components and the electrode. The combined resistance of grain boundary and grains is considered to be the overall sample resistance. Unfortunately, the use of IS for quantifying β'' -alumina does not follow the ideal Nyquist plot seen above; the range at which the sample effects would be seen is outside the frequency capability of the instrument. The data observed after experimental IS only shows the effect of the electrode on impedance data. However, it is possible to extrapolate the plotted Z' vs. Z'' data to determine the point at which the data intercepts the Z'' axis, allowing for the approximation of the sample resistance.

Samples with basic geometries, such as pellets, are measured somewhat easily in the IS setup. A sintered sample is sandwiched between two blocking electrodes. A conductive paste is applied directly to both faces of the sample, aligned in parallel, so that the distance between the faces of the electrodes is the thickness of the sample itself. This electrode paste provides for an electrode in intimate contact with the sample of known area. Next, a foil electrode is 'glued' to the painted electrode with the addition of more conductive paste. This allows for a robust interface between the painted electrode and the leads of the instrument. Once the resistance of a sample is obtained through the use of IS, its resistivity can be determined using electrode area and path length i.e. sample thickness. The calculation is outlined below in Equation 7.

$$\rho = R \left(\frac{A}{L} \right) \quad (7)$$

ρ = Sample resistivity ($\Omega \cdot \text{cm}$)

A = Electrode area (cm^2)

L = Sample thickness (cm)

The reproducibility of two probe IS using different blocking and non-blocking electrode materials for β and β'' -alumina has been investigated in several studies. Gold, silver, platinum and sodium electrodes have all been evaluated. For IS measurements of β -alumina, the results have been mostly consistent.^{3, 25, 51} It has been observed that the activation energy is somewhat stable over a wide range of temperatures with varying electrode materials, as determined through the use of Arrhenius plots. However, the use of different electrode materials on IS measurements of β'' -alumina materials has been less conclusive.⁵²

III. EXPERIMENTAL PROCEDURE

A. Powder Synthesis

Synthesizing materials with the desired composition and favorable powder properties can be quite complicated. Although there are several approaches that can be used, ultimately, the Sudworth process was selected as the most reliable synthesis route.¹⁶ Although somewhat intricate, this processing method allowed for a fully formed β'' -alumina powder with good flow behavior and normal distribution of granule size, all of which affect the sintered product.

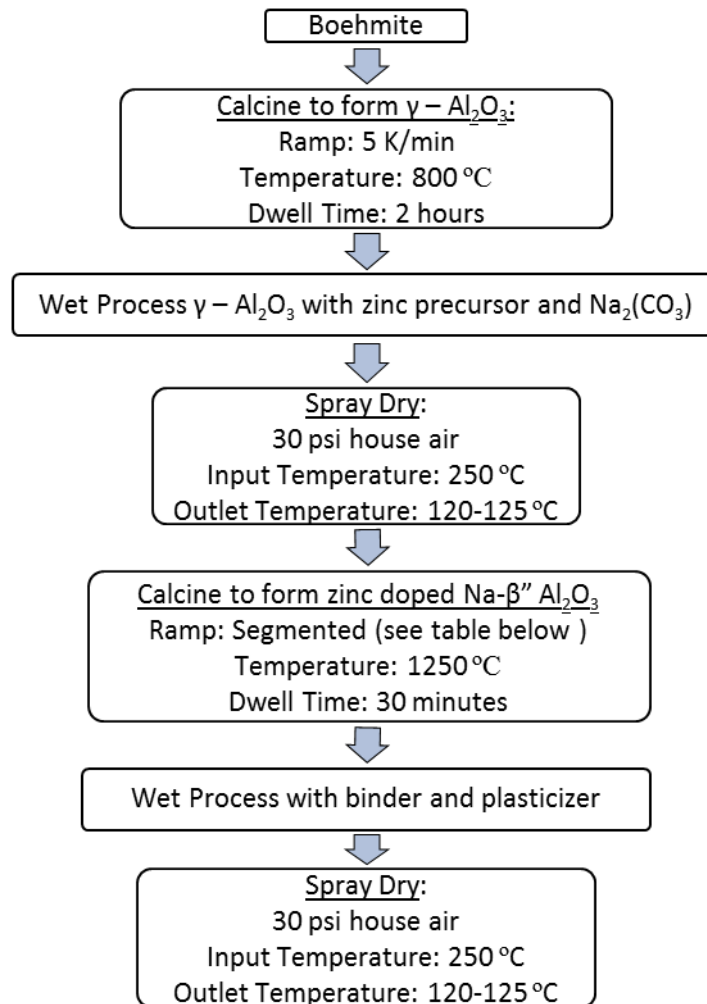


Figure 6. Flow chart depicting the processing route used to make zinc doped Na β'' -alumina used in this research.

Figure 6 depicts the processing steps used to synthesize the desired powder compositions. First, boehmite ($\text{AlO}(\text{OH})$), a hydrated form of aluminum oxide, was calcined to $800\text{ }^{\circ}\text{C}$ and held at temperature for 2 hours. This allowed for all adsorbed and chemically bonded water to be removed from the material. Dehydration of boehmite resulted in the formation of γ -alumina, which served as the alumina precursor for the composition. Gamma alumina is a desirable alumina precursor for two reasons. First, the presence of vacancies on cationic sites in the material allows for both stabilizing and transporting ions to be absorbed into the structure relatively easily. Second, gamma alumina has a spinel structure very similar to that of the desired beta alumina phase, making it easier to synthesize the correct phase during calcination.

The gamma alumina was wet processed with the remaining components of the batch; zinc acetate dihydrate ($(\text{Zn}(\text{C}_2\text{H}_3\text{O}_2)_2 \cdot 2\text{H}_2\text{O})$), sodium carbonate monohydrate ($\text{Na}_2\text{CO}_3 \cdot \text{H}_2\text{O}$), and Darvan 811 (Na-PAA). Zinc acetate was used to introduce zinc into the batch while sodium carbonate introduced sodium. Both precursors were chosen based on their favorable solubility limits in water. The addition of Darvan 811 was solely for the dispersion of alumina during wet processing. It should be noted that heat treatments were performed on all precursors prior to batch calculation to accurately account for the loss on ignition (LOI) that occurs during the second calcining procedure. Specified batching sheets that include all relevant variables were used when calculating batch compositions in order to meet batch composition targets. These batch sheets can be found in the appendix.

A procedure for wet processing was performed as follows. First, dispersant was added to the desired amount of deionized water and allowed to mix using a sheer mixer (Johnson Tool Design, Cortland, NJ). Next, γ -alumina was added, followed by the zinc acetate and lastly the sodium carbonate. Between each material addition, the batch was allowed to mix for several minutes. After all constituents were added, the batch was mixed for several minutes prior to milling for 1 hour in a vibratory mill (Sweco, Florence, KY) using alumina media. Finally, spray drying was performed (Bowen NozzleTower Mixed Flow Dryer, GAE Process Engineering, Columbia, MD). This allowed for the production of a homogeneous powder in which each spray dry granule

was representative of the overall batch chemistry. The parameters used for spray drying can be found in Figure 6.

After spray drying, the powder was calcined to form the desired zinc doped Na β' -alumina phase. Fully calcining the powder was somewhat difficult due to the large amount of organic material that needed to be removed during heat treatment. The goal was to calcine the material, while still removing all desired organic material. Sintering steps and rates were initially based on TGA measurements performed on the uncalcined spray dried granules (available in the appendix). Several adjustments were made to the original calcination cycle to obtain full organic burnout. The resulting calcining procedure is seen in Table II below.

Table II. Calcining Procedure for Formation of Zinc Stabilized Na β' -Alumina Phase with No Organics Remaining

Ramp Up				
Segment	Range (°C)	Set Point (°C)	Ramp Rate (K/min)	Dwell Time
1	35-230	230	2.0	-
2	230-370	370	0.4	-
3	370-420	420	1.5	-
4	420-550	550	0.2	-
5	550-750	750	0.5	-
6	750-1250	1250	3.0	-

Dwell				
Segment	Range (°C)	Set Point (°C)	Ramp Rate (K/min)	Dwell Time
7	n/a	1250	n/a	30 min

Ramp Down				
Segment	Range (°C)	Set Point (°C)	Ramp Rate (K/min)	Dwell Time
8	n/a	35	3.0	-

A specific procedure for powder containment during calcining was also followed. Powders were placed inside high purity MgO crucibles with MgO lids that were ground to fit using 300 grit SiC powder. This was an important step as it allowed for an intimate seal between crucible and lid, which helped minimize sodium loss during calcination. A small piece of graphite paper was used to prop open the lid of the crucible prior to calcining. This allowed for the release of organic materials from the crucible at low

temperature, but vaporized at higher temperatures, closing the lid and minimizing sodium loss occurring at higher temperature. Additionally, this helped decrease pressure build up inside the crucible which occurred during the organic burnout window at lower temperatures.

After calcination, another wet processing and spray drying step was performed to introduce a binder and plasticizer into the powder, resulting in better powder flow behavior and increased green strength. Binder and plasticizer could not be introduced prior to calcining as they would have burned out during heat treatment. The wet processing procedure was similar to the initial wet processing of the precursors. Calcined powder was added to deionized water followed by the binder (Airvol 205 PVA; 30-51k molecular weight) and plasticizer (PEG-400). This suspension was milled for 1 hour and spray dried using the same parameters found in Figure 6. This resulted in the synthesis of a homogenous zinc doped Na β '-alumina with favorable powder flow and die fill.

B. Sample Forming

Once the specific powder compositions were synthesized, compacts of these powders were formed. First, a desired amount of sample was weighed out. The specific mass of powder used for each sample was dependent on the desired thickness of the sample after sintering. A variety of sample thicknesses were needed to perform the different impedance spectroscopy experiments utilized throughout the course of this work. Sample thickness for the 'electrode material study' varied from 1-5 mm, therefore samples of different masses were pressed creating a range of sample thicknesses. The desired thickness for the 'excess soda & sintering study' was determined to be 3 mm. This thickness was chosen to mitigate the potential for variation in impedance data that has been observed in thinner (≤ 1 mm) samples. Sintering studies showed that 0.6 grams of unsintered powder yielded roughly 1 mm of sintered compact. This correlation scaled linearly and was used to press pellets of varying sintered thicknesses.

Sample pellets were pressed uniaxially using a hydraulic Carver press (Carver Inc., Wabash, IN) and a stainless steel die. The round die utilized two independent plungers, 5/8 inches in diameter. Powders were pressed to 5 kPsi to shape the sample pellets. Thinner (0.8 mm) samples used as setters during sintering were also pressed at

this time. All samples were placed in between pieces of felt and vacuum sealed inside FoodSaver® bags to create a ‘wet bag’ for isostatic pressing. Pellets were grouped and sealed in bags according to sintering cycle. Samples were pressed isostatically in a 4 inch diameter isostatic press (Ilshin Autoclave, Deajeon South Korea) to 18 kPsi for 60 seconds at pressure.

C. Sintering of Samples

1. Sintering Setup

Sintering beta alumina (both β and β'') can be somewhat problematic due to the increased volatility of sodium at high temperatures. A special setup was used to mitigate sodium loss and create samples with largely unmarred surfaces which were needed for impedance spectroscopy measurements. A closed crucible was used in conjunction with sodium-containing sacrificial powder to create a sodium-rich environment. This encouraged soda loss from the sacrificial powder rather than from the sintered sample. For purposes of this thesis, unsintered powder matching the composition of the sintered sample was used as sacrificial material. To create the necessary sintering environment, a high-purity MgO crucible with a ground MgO lid was used. The intimate fit between the crucible and lid minimized sodium loss from the crucible during sintering. The crucible lid and lip were cleaned with isopropyl alcohol prior to sintering to ensure the best fit.

Although the presence of a sacrificial soda powder was important to the sintering environment inside the crucible, it was also somewhat problematic. If a traditional powder bed (covering the entire bottom of the crucible) was used, granules of sacrificial powder would sinter onto the surface of the sample pellet, causing a rough texture. This roughness is not optimal for impedance spectroscopy testing and therefore was avoided. One way to avoid this surface roughness was to use sacrificial pellet pieces. To accomplish this, sample pellets were propped up on small pieces of unsintered setter pellets (with the same composition as the sample) in the middle of the crucible and were then surrounded by a ring of sacrificial powder. This created the desired sodium rich environment with minimal surface damage to the sample pellets.

2. Sintering Parameters

Sintering of samples was performed in a Carbolite HTF 17/10 furnace (Carbolite, Hope Valley United Kingdom) utilizing molybdenum disilicide elements. Sintering parameters varied depending on the sample's intended use. Sintering parameters for samples used in the electrode materials study were held constant. These samples were sintered to 1625 °C for 30 minutes using a 3 K/minute ramp rate. Samples used for the excess soda study were sintered at a variety of temperatures and times. Three different sintering temperatures (1610 °C, 1625 °C and 1640 °C) and two different dwell times (30 minutes and 1 hour) were utilized. All samples were sintered with a ramp rate of 3 K/minute and a cooling rate of 5 K/minute.

D. Density Measurements

One sintered sample was selected at random from each sample set containing different sintering parameters for each composition. Sample density was measured via immersion density. The ASTM standard C830-00 was followed with only minor alterations. Dry weight was measured prior to placing samples in a beaker of kerosene. Samples were then placed under vacuum for 1-2 hours to fully infiltrate any porosity. Suspended weights were measured using kerosene as well. Samples were blotted lightly with a lint-free tissue to remove excess kerosene from the sample surface prior to measuring saturated mass.

The bulk density of samples was determined using equation 8:

$$\rho_{Bulk} = \left[\left(\frac{D}{S - W} \right) * \rho_{Liquid} \right] \quad (8)$$

ρ_{bulk} = sample's bulk density (g/cm³)

D = Sample dry mass (g)

S = Samples saturated mass (g)

W = Sample suspended weight (g)

ρ_{liquid} = Specific gravity of immersion liquid (g/cm³)

The density of kerosene varies slightly, so density of this particular kerosene was measured to increase calculation accuracy. A 100 ml pycnometer cup was filled with kerosene and the mass used to measure density. This was done three times. It was found that the average density of this specific kerosene was 0.8295 g/cm³. This density was then used to determine the density of the sintered samples.

To determine the percent theoretical density of sintered pellets, bulk powder density was obtained. Powder of each composition was collected after calcining, but prior to the addition of binder and plasticizer, and bulk powder density was measured using an AccuPyc II 1340 He-pycnometer (Micromeritics, Norcross, GA)

E. SEM

1. Sample Preparation and Imaging Conditions

One sample from each sample set was selected at random for microstructural analysis. Samples were mounted in thermoplastic cement (Buehler Ltd, Lake Bluff, IL). Once mounted, samples were ground and polished using progressively finer SiC paper. Once polished, samples were thermally etched to enhance topography and accentuate grains. The procedure for thermal etching involved heat treating sintered samples at a temperature 50 K below the sample's sintering temperature for 30 minutes. Heating and cooling rates during thermal etching were 5 K/minute.

Polished etched surfaces were viewed using an Environmental Scanning Electron Microscope; or ESEM, (Quanta 200F, FEI Co., Hillsboro, OR). Three fields of each polished surface were captured at several different levels of magnification to obtain a thorough sampling of grain and microstructure images. Imaging conditions are listed in Table III.

Table III. SEM Imaging Conditions Used to Obtain Photomicrographs

Accelerating Potential	Spot Size	Working Distance	Vacuum Setting	Signals Collected
20 keV	3	9 -10 mm	High Vac.	SE, BSE, Combined

2. Grain Size Analysis

Analysis of photomicrographs was performed in accordance with ASTM Standard E112-10, which gives standard test methods for the determination of average grain size. In this case, systematic point count was used with the intercept method. Three templates, each with 10 straight lines randomly drawn across the field were created in Photoshop CC 2015 (Adobe, San Jose, CA) and the line lengths (calibrated to the size bar) were measured using ImageJ Version 1.47 (National Institute of Health, Bethesda, MD). The template was applied to a microstructural image and a systematic point count was performed for each line, which allowed for the calculation of average grain diameter. This process was performed on every microstructural image using all three templates. Values were averaged together to obtain a representative grain size.

F. Impedance Spectroscopy

1. Sample Preparation and Equipment Operation

Impedance spectra were collected using an SI 1260 Impedance/Gain-phase analyzer (Solartron Analytical, Farnborough, United Kingdom) connected to an ET3216/WhipMix furnace (Whip Mix Corporation, Louisville, KY). Measurements at temperature were achieved by coordinating both the furnace and analyzer using LabVIEW (National Instruments, Austin, TX) and a house-built control system. The furnace profile was loaded into the LabVIEW software prior to testing. Data were collected over a range of temperature, 250 °C - 350 °C, at 5 K intervals. Samples of the highest temperature were measured first, and furnace temperature was decreased as data was collected over the range.

Prior to loading the sample, an initial frequency sweep was performed at ambient temperature with the solid foil electrodes shorted, i.e. with no sample between them. This allowed for the resistance of the solid electrode and instrument leads to be determined and eventually subtracted from the collected sample data. To do so, the two solid electrodes were placed between the furnace's platinum leads and a sweep was performed using the ZPlot (Solartron Analytical, Farnborough, United Kingdom) software. Sweep parameters are listed in Table IV.

Table IV. Sweep Parameters for Closed Circuit Measurement

DC Potential (Volts)	AC Amplitude (mV)	Initial Frequency (Hz)	Final Frequency (Hz)	Sweep Type	Interval	Interval Type	Sweep Direction
0 [Applied E]	100	1×10^7	1000	Logarithmic	10	Steps/ Decade	High frequency to low frequency

After the initial sweep, collected data were fit to an equivalent circuit using the ZView (Solartron Analytical, Farnborough, United Kingdom) software. A resistor and an inductor were placed in series and approximate values for each were inputted with an allowed +/- freedom level. The approximate resistor and inductor values were 0.005 ohms and 2.0×10^{-8} H, respectively. Equivalent circuit fitting yielded exact values for each. The fitting parameters are shown in Table V.

Table V. Fitting Parameters for Equivalent Circuit Data

Mode	Data Range	Max Iterations	Optimization Intervals	Type of Fitting	Type of Data Weighing	GDAE Accuracy	Absolute Temp.
Fitting	All Points	100	0	Complex	Calc. Mode	2	293

Particular care was taken to ensure that sample electrodes were parallel and well aligned. Prior to measurements, a special stencil was constructed that sandwiched the sample, and allowed for the electrode perimeter to be drawn onto the sample with a mechanical pencil. This also kept the electrode area constant. Electrodes were placed in the middle portion of the sample, as close to the center as possible. Once the electrode was drawn on, the electrode was painted on with a fine brush using the desired paste material. Once the electrode paste was dry, a small amount of paste was then used to secure the solid electrode on top of the painted electrode. Electrode diameter size was 7.6 mm in diameter. Sintered sample size was roughly 15 mm in diameter and 1-5 mm thick, depending on sintering and experiment type.

Next, the sample was placed in between the platinum leads of the IS fixture, and the sample tested to ensure a proper connection had been achieved between the sample and the instrument. To do this, an additional sweep was performed at ambient temperatures using the same parameters used to test the solid electrodes. If a good

connection was present, a line with a positive slope was observed on the collected Z' vs. Z'' plot. If a good connection was not made, a vertical or erratic line appeared on the plot. An example of both a good and bad connection can be seen in Figure 7 and Figure 8.

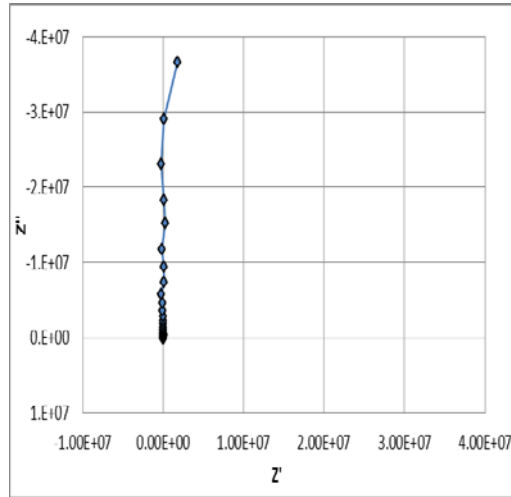


Figure 7. Quick sweep impedance data illustrating poor sample connection.

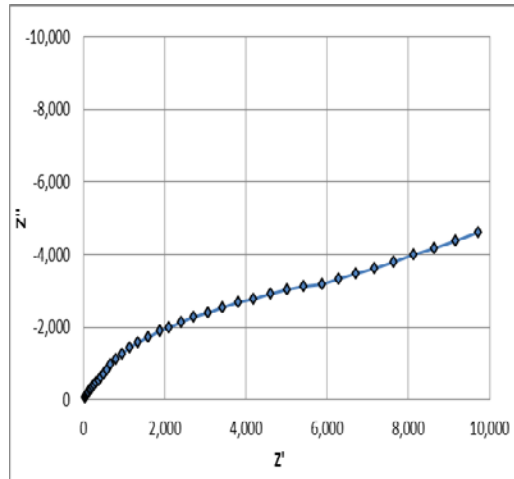


Figure 8. Quick sweep impedance data illustrating good sample connection.

If a good connection was not achieved, the leads were repositioned and an additional frequency sweep was performed to recheck the connection. Once a proper connection was achieved, the sample was ready for testing. Samples were tested at a temperature range of 350 °C to 250 °C in 5 K increments. At each desired temperature,

impedance data were collected by sweeping from high frequency to low frequency using the parameters in Table V.

Table VI. Impedance Sweep Parameters Used to Collect Sample Data

Zmeter Setup	Sweep Type	Start Freq.	Stop Freq.	Data Points	Voltage Bias	Voltage Amp	Circuit	I Range	V1 Range
Uncompensated	Log. Freq.	10 M	10 k	62	0	0.1	Parallel C, R	Auto	Auto

Once sample data were collected, equivalent circuit values were used to correct for the impedance from the equipment leads and solid electrodes. This correction was done on the sample data using MatLab (MathWorks, Natick, MA). The specific code can be found in the appendix. To increase the accuracy of the data, solid electrodes were tested and the equivalent values were obtained prior to every sample measurement, in order to account for a slight variation in electrode/lead resistance between runs. The difference in compensated and uncompensated impedance data is shown in Figure 9. The contribution of lead and electrode resistance is evident from data points that exhibited positive Z'' values.

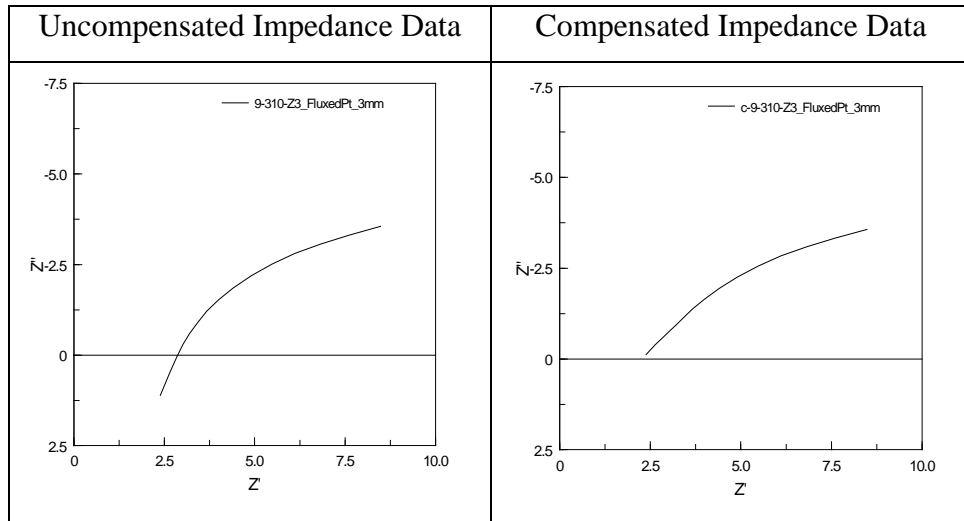


Figure 9. Examples of raw uncompensated and compensated impedance data.

2. Data Analysis

The interpretation of impedance data presented some challenges. Ideally, impedance data can be analyzed using equivalent circuit modeling, as illustrated in Figure 5. Unfortunately, the impedance data collected in this work did not contain enough information (features) to enable equivalent circuit modeling. Instead, an extrapolation technique was developed to determine sample resistance.

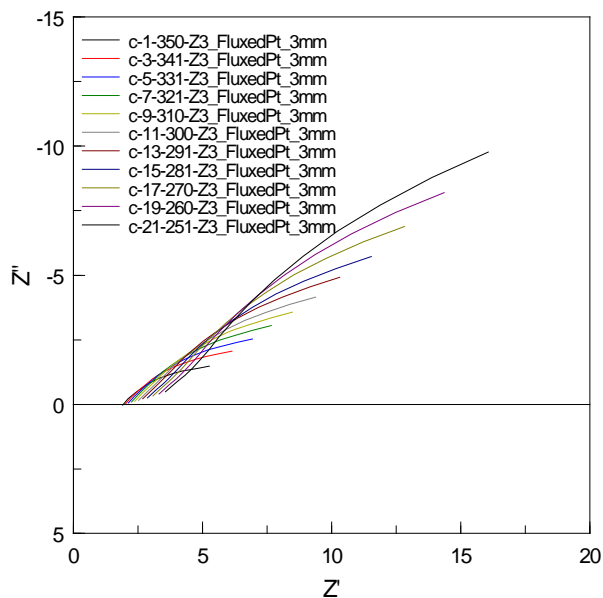


Figure 10. Representative impedance spectra for sintered samples.

Figure 10 shows a representation of the compensated spectra collected over a range of temperatures, 250 °C - 350 °C. In these spectra, semicircles (arcs) corresponding to the sample grain and grain boundary response are not seen because the response range lies above the upper frequency limit of the instrument. The data observed in Figure 10 was interpreted as the electrode-interface arc and the intersection of this “line” with the x-axis is interpreted as the resistance contributed by the sample. In most cases, the data did not intersect the horizontal, so the data needed to be extrapolated to the horizontal axis to determine the sample resistivity. This was accomplished through the use of a linear trend line fit to the data, where the equation of the line was provided by the software. For most samples, the resistance value obtained from extrapolating to the horizontal axis was

depended on how many data points were used. Figure 11 shows how the number of data points taken into consideration when extrapolating to the x-axis affects the interpreted sample resistance.

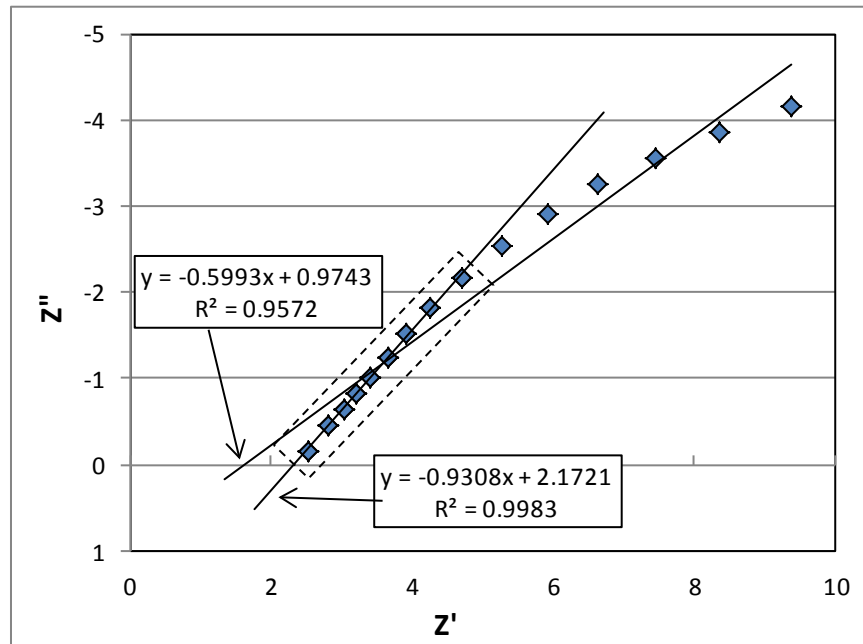


Figure 11. The effect of the number of data points used determined resistance.

In most cases, the data did not exhibit a linear trend over the entire range. This is evident when examining the fit of trend lines to the data set, represented by the trend line's R^2 value. An R^2 value of 1.0 indicates a perfect fit of the trend line to the data; values <1.0 indicate a non-perfect fit, where the smaller the R^2 value the worse the fit. This is shown in Figure 11. If all collected data points were used to fit the trend line, a poor fit occurred ($R^2 = 0.957$) and the obtained sample resistance was lower than the actual sample resistance. However, if a smaller range of data was used to fit the linear trend line, a much better fit was obtained ($R^2 = 0.998$), which gave a more accurate representation of sample resistance. Therefore, the goal was to use enough data points to be representative of the sample, while still maintaining a good fit by the trend line. The following method described below was developed in an attempt to reduce the subjectivity of selecting a data range for the extrapolation.

Data were collected by the solartron and automatically saved in a spreadsheet with columns of data that included Z' and Z'' . These data were considered uncompensated because the contribution of lead and electrode resistance had not yet been subtracted from them. As previously stated, this compensation was done using MatLab which produced new spreadsheets files with columns of corrected Z' and Z'' data. The Excel program was used to calculate the running slopes and running intercepts of the Z' vs. Z'' data, starting with the high-frequency data. Next, an R^2 value was calculated to represent how well the running slope fit the Z' vs. Z'' data at that given point. Another running calculation was used to obtain a resistance value from the corresponding slope and intercept values that had been calculated for that given frequency. Lastly, a running standard deviation was performed to monitor the standard deviation of the resistance values in the set up until the given frequency. A copy of an example Excel sheet with annotated formulas are shown in Figure 12.

Compensation: Rp=1.0e+08,Cp=6.0e-12,Rs=0.008,Is=2.49e-08												
Temp: 340.2												
Data Point	62											
Freq(Hz)	Z'	Z''	Z	Theta	Spot Freq	Cp	D	SLOPE	INT	Rsq	R Value	stdev
1.00E+07	2.15E+00	-3.37E-01	2.17E+00	-8.9E+00	1.00E+03	6.62E-07	1.92E+00	-1.59892	3.09269	1	1.93423	
8.95E+06	2.33E+00	-6.34E-01	2.42E+00	-1.5E+01	0.00E+00	0.00E+00	0.00E+00	-1.5525	2.99045	0.99961	1.92621	0.29317
8.00E+06	2.48E+00	-8.58E-01	2.63E+00	-1.9E+01	0.00E+00	0.00E+00	0.00E+00	-1.52485	2.9281	0.99952	1.92026	0.36412
7.16E+06	2.61E+00	-1.05E+00	2.82E+00	-2.2E+01	0.00E+00	0.00E+00	0.00E+00	-1.52031	2.91765	0.99971	1.91912	0.36055
5.40E+06	2.72E+00	-1.22E+00	2.99E+00	-2.4E+01	0.00E+00	0.00E+00	0.00E+00	-1.48868	2.84329	0.99907	1.90994	0.46918
5.73E+06	2.85E+00	-1.38E+00	3.17E+00	-2.6E+01	0.00E+00	0.00E+00	0.00E+00	-1.46493	2.78638	0.99881	1.90206	0.59882
5.13E+06	2.96E+00	-1.53E+00	3.34E+00	-2.7E+01	0.00E+00	0.00E+00	0.00E+00	-1.4505	2.75122	0.99889	1.89674	0.70045
4.58E+06	3.06E+00	-1.68E+00	3.49E+00	-2.9E+01	0.00E+00	0.00E+00	0.00E+00	-1.43193	2.70509	0.99871	1.88913	0.81526
4.10E+06	3.18E+00	-1.83E+00	3.67E+00	-3.0E+01	0.00E+00	0.00E+00	0.00E+00	-1.4131	2.65745	0.9985	1.88059	0.94743
3.67E+06	3.31E+00	-1.99E+00	3.87E+00	-3.1E+01	0.00E+00	0.00E+00	0.00E+00	-1.39871	2.62044	0.9985	1.87346	1.07528
3.28E+06	3.43E+00	-2.16E+00	4.06E+00	-3.2E+01	0.00E+00	0.00E+00	0.00E+00	-1.38638	2.58816	0.99854	1.86685	1.19539
2.94E+06	3.56E+00	-2.32E+00	4.25E+00	-3.3E+01	0.00E+00	0.00E+00	0.00E+00	-1.37314	2.5529	0.99851	1.85916	1.31936
2.63E+06	3.70E+00	-2.50E+00	4.46E+00	-3.4E+01	0.00E+00	0.00E+00	0.00E+00	-1.3572	2.50961	0.9983	1.84911	1.46424
2.35E+06	3.86E+00	-2.68E+00	4.70E+00	-3.5E+01	0.00E+00	0.00E+00	0.00E+00	-1.34011	2.46235	0.99803	1.83743	1.63649
2.10E+06	4.03E+00	-2.88E+00	4.96E+00	-3.6E+01	0.00E+00	0.00E+00	0.00E+00	-1.3223	2.41219	0.99772	1.82424	1.8386
1.88E+06	4.22E+00	-3.09E+00	5.23E+00	-3.6E+01	0.00E+00	0.00E+00	0.00E+00	-1.30552	2.36406	0.9975	1.81082	2.06389
1.68E+06	4.41E+00	-3.31E+00	5.52E+00	-3.7E+01	0.00E+00	0.00E+00	0.00E+00	-1.28978	2.31809	0.99736	1.79728	2.30578
1.51E+06	4.61E+00	-3.54E+00	5.81E+00	-3.8E+01	0.00E+00	0.00E+00	0.00E+00					
1.35E+06	4.82E+00	-3.77E+00	6.12E+00	-3.8E+01	0.00E+00	0.00E+00	0.00E+00					
1.20E+06	5.05E+00	-4.02E+00	6.46E+00	-3.8E+01	0.00E+00	0.00E+00	0.00E+00					
1.08E+06	5.31E+00	-4.28E+00	6.82E+00	-3.9E+01	0.00E+00	0.00E+00	0.00E+00					
9.64E+05	5.59E+00	-4.56E+00	7.21E+00	-3.9E+01	0.00E+00	0.00E+00	0.00E+00					
8.62E+05	5.89E+00	-4.85E+00	7.63E+00	-3.9E+01	0.00E+00	0.00E+00	0.00E+00					
7.71E+05	6.22E+00	-5.15E+00	8.07E+00	-4.0E+01	0.00E+00	0.00E+00	0.00E+00					
6.90E+05	6.57E+00	-5.47E+00	8.55E+00	-4.0E+01	0.00E+00	0.00E+00	0.00E+00					
6.17E+05	6.94E+00	-5.79E+00	9.04E+00	-4.0E+01	0.00E+00	0.00E+00	0.00E+00					

Excel Formula (n=row number)	
SLOPE	"=SLOPE(C58:Cn,B58:Bn)"
INT	"=INTERCEPT(C58:Cn,B58:Bn)"
Rsq	"=RSQ(C58:Cn,B58:Bn)"
R Value	"=-ln/ln"
St. Dev	"=STDEV(L59:Ln)/L(n-1)*100"

Figure 12. Sample Excel spreadsheet used to organize raw data and determine sample resistance at a given temperature.

The standard deviation column was examined to find where the standard deviation became greater than or equal to one percent of the measured R value. This value was chosen in order to highlight the point at which the inclusion of new data points

became detrimental to the fit of the trend line; at which point only the previous data range was used to determine the resistance of the sample. The resistance value that corresponded to this point in the data was taken to be the absolute resistance of the sample at that particular measurement temperature. This protocol was followed as a means to determine resistance using the most data points while still maintaining a low standard deviation between data. It was found that if resistance calculations were based on too many data points in the series then the data became inconsistent and therefore unreliable, as demonstrated in Figure 11. This procedure was repeated for all data sets over the temperature range (250 °C–350 °C). This resulted in a condensed representation of sample resistance as a function of temperature. It was found that analyzing the data in 10 K intervals gave a good representation of the data and cut down on the amount of time needed to analyze data. Although resistance and resistivity values were obtained for samples over a range of temperatures, most data used for analysis came from measurements taken at 300 °C. Figure 13 shows how data were condensed and graphed on an Arrhenius plot; to evaluate the sample performance across the range of temperatures.

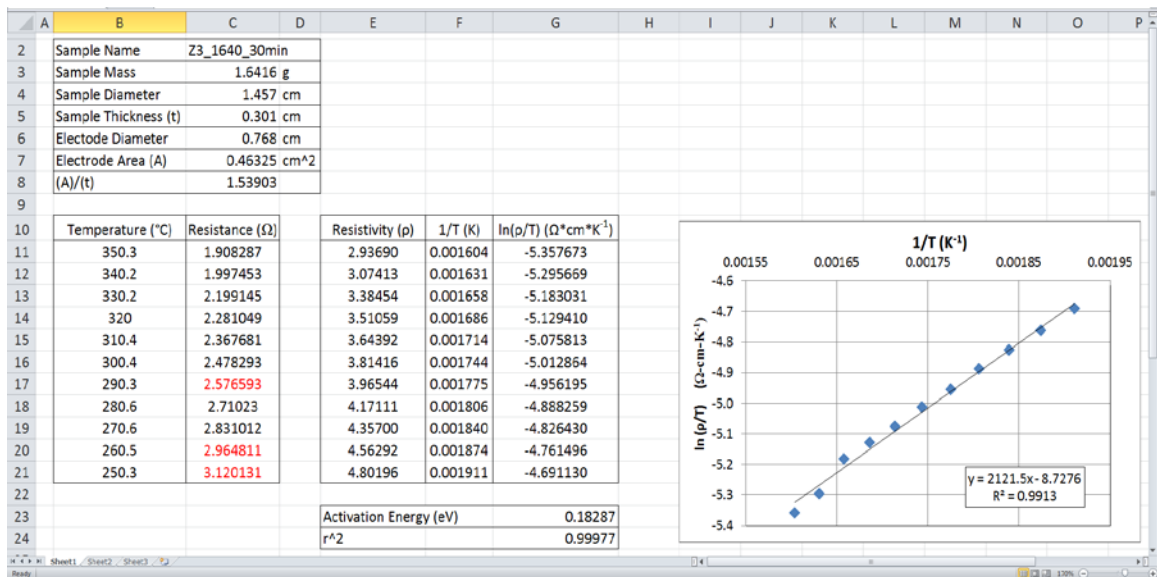


Figure 13. Sample of condensed electrical data for one sample over the desired temperature range.

The Arrhenius theory is applicable to ionic conductors due to their electrolytic nature. Therefore, Arrhenius behavior can be used to determine the activation energy of ionic conductivity mechanisms within the material. The Arrhenius equation is shown below in Equation 9. The modified Arrhenius relationship which utilized resistivity instead of conductivity is shown in Equation 10.

$$\sigma = \left(\frac{\sigma_o}{T} \right) e^{-Ea/kT} \quad (9)$$

$$\ln\left(\frac{\rho}{T}\right) = \left(\frac{Ea}{k}\right)\left(\frac{1}{T}\right) + \ln(\rho_o) \quad (10)$$

σ = Conductivity (Ohms*cm)⁻¹

T = Temperature (K)

Ea = Activation Energy (eV)

k = Boltzmann's Constant (eV/K)

ρ = Resistivity (Ohms*cm)

Plotting resistivity data on an Arrhenius plot with axes $\ln(\rho/T)$ vs. $(1/T)$ allowed for the activation energy of the conduction mechanism in the material to be determined. By rearranging the variables and substituting for resistivity, the Arrhenius equation could be related to the equation of a straight line; $y = mx+b$. In this way, the $\ln(\rho/T)$ term was thought of as “y,” $(1/T)$ was “x,” $\ln(\rho_o)$ was the y-intercept “b” and E_a/k was the slope of the line. When plotted in this way, determining the slope of the line created by the data allowed for the back calculation of activation energy using Boltzmann's constant.

Impedance spectroscopy measurements for this study were performed on a variety of samples in support of two main investigations. The first objective was to test the electrical properties of zinc stabilized β' -alumina while varying two parameters, sintering and powder composition. The second objective was to evaluate the effect of different electrode materials on the impedance spectroscopy measurements themselves, and to evaluate whether the different materials could yield consistent, reliable results.

To evaluate the effect of electrode material on impedance measurements, four different electrode materials were selected. As previously discussed, both a paste and a solid component were utilized to create the electrode that acted as an interface between the sample and the instrument leads. Four different sample pastes and three solid components were used to create four separate sampling conditions. These conditions can be seen in Table VII.

Table VII. Parameters for Diffraction Experiments Performed on Powder and Solid Samples

Condition Number	Electrode Paste Material	Constituents	Solid Electrode Material
1	Fluxed Platinum	Platinum, Bismuth Hydroxide, Terpeneol	Platinum Metal
2	Unfluxed Platinum	Platinum, Terpeneol	Platinum Metal
3	Gold	Gold, Terpeneol	Gold Metal
4	Carbon	Colloidal Graphite, Isopropyl Alcohol	Carbon Paper

For the electrode material study, these four conditions were used to measure a variety of samples, each sintered under the same conditions and pressed from the same powder composition. The only variables that were altered were the electrode material and sample thickness. However, samples that were tested to investigate the effects of sintering and composition on electrical properties were treated somewhat differently. These samples were made of different powder compositions sintered at different sintering parameters. The one parameter in this case which was held constant was which electrode material was used to perform the impedance spectroscopy measurements. For this sample set, only one electrode setup was used; bismuth fluxed platinum paste in conjunction with a solid platinum metal electrode.

G. XRD

X-Ray diffraction was performed on both powder and solid sintered samples. For powder samples, a plastic sample holder was used and powder was pressed into the grooves until flat and level with the surface of the holder. For solid samples, again a plastic sample holder was used with conjunction with carbon putty to hold samples even

with the edge of the sample holder. This mitigated the effects of sample displacement. Measurements were performed using a Bruker D8 (Bruker AXS, Germany) diffractometer with a linear position sensitive detector. Jade 9 (Port of Los Angeles, CA) was used for phase identification and peak area calculations. The parameters for the diffraction experiment are listed in Table VIII.

Table VIII. XRD Measurement Parameters

Radiation Type	Degrees 2θ Range	Step Size (Degrees 2θ)	Dwell Time (seconds)
Cu $K\alpha$	5 – 70	0.0195	2

H. ICP

ICP MS analysis was performed by ACME (Bureau Veritas Mineral Laboratories, British Columbia, CN). Powder samples were dissolved by the organization on site. Na_2O , and Al_2O_3 and Zn analytes were reported after analysis.

IV. RESULTS AND DISCUSSION

A. Effect of Electrode Material on Impedance Spectroscopy Measurements

Four different materials were used as electrodes for impedance spectroscopy measurements: bismuth-fluxed and unfluxed platinum, gold, and carbon. These electrodes were used to measure sintered samples ranging in thickness from 1 to 5 mm. The composition and sintering conditions of these samples were kept constant; samples of composition Z3, sintered at 1625 °C for 30 minutes were used. This allowed for the evaluation of the electrode materials themselves without the effect of sample variation. This also allowed for the effects of sample thickness on impedance spectroscopy measurements to be evaluated.

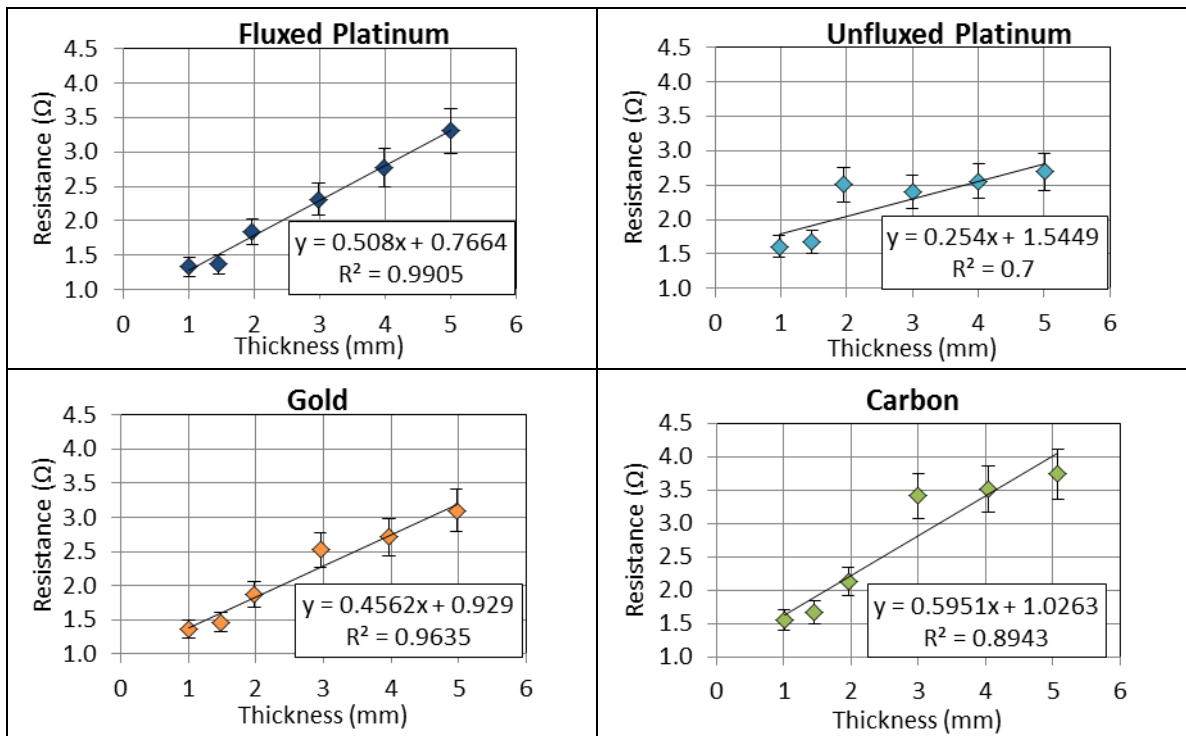


Figure 14. Resistivity vs. thickness for samples of different thicknesses measured using four different electrode materials at 300 °C. Linear trend lines were fit to the data with varying success (see text).

Figure 14 shows the effect of sample thickness on sample resistance for each of the four different electrode materials at 300 °C. Data taken at 300 °C are often used as a reference point for resistance measurements. This stems from the use of such materials in batteries that usually operate at elevated temperatures. Error bars in the figure represent a 10% uncertainty, which is the estimated uncertainty in the impedance measurements at the frequency and resistance measured. Resistance values come from the interpretation of data as outlined in the experimental procedure. Resistance is a bulk measurement and therefore does not represent an intrinsic material property. Sample thickness has a direct effect on the measured resistance; the thicker a sample, the larger the measured resistance. This is explained using Equation 7, which shows the direct relationship between sample thickness (L) and resistance (R). This correlation was shown in Figure 14. An increase in resistance was measured as the thickness of samples was increased. This trend appeared to be a linear relationship and was represented with trend lines fit to each data set.

Although the data followed trends that one would expect to see, there were a few interesting deviations of note. Experimental data for the four electrode plots were displayed with identical axes to highlight the differences between data sets. It was observed that although resistances for 1 mm samples were relatively similar for all four electrode materials, the resistance values began to vary as sample thickness was increased. This was evident by the different slopes observed for the four different sets of data. Preliminarily, this suggested that the data obtained from impedance spectroscopy measurements conducted using different electrode materials were not relatable to each other. However, another artifact of the collected data indicated that further corrections needed to be made. Linear trend lines fit to each of the four data sets all indicated the y-intercept of the data to be noticeably larger than zero. This was problematic because it suggested that for a sample with zero thickness, there would be a non-zero resistance measured, which would not be expected. Therefore it was assumed that some contributing factor in the data had not been taken into consideration.

In electronic conductors tested under DC conditions, a positive y-intercept in R resistance vs. temperature data is often referred to as a contact resistance. The term refers to a specific condition of electronically conductive materials where the energies of the

bands in the electrode and sample materials become misaligned as their Fermi levels align. This causes an additional resistance to be measured by the instrument regardless of sample resistance. This definition is applied to electrical conductors and the effect in ionic conductors with blocking electrodes requires further investigation. In this work, we will refer to the observation of a positive y-intercept as “contact resistance,” although the source of this phenomenon is not well understood. Typically impedance spectroscopy is used to eliminate the effect of such phenomena. Therefore it is somewhat intriguing that we see such an effect in these data.

As the deviation in data at zero thickness was attributed to a contact resistance, quantifying the effect and magnitude of this resistance present during sample measurement was important. This allowed for the calculation of true sample resistance from the data. Figure 15 shows an example of the method used to determine the contact resistance in this work.

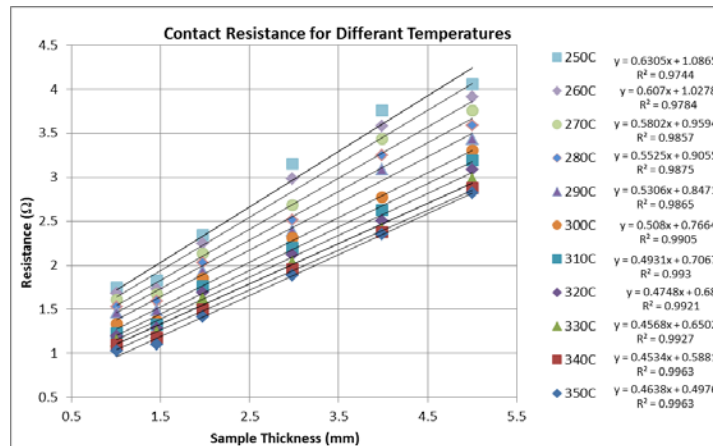


Figure 15. Example of the graph used to determine the contact resistance for samples over a range of temperatures.

The data shown in this specific plot were collected using the fluxed platinum electrode. Overall it is observed that as the measurement temperature increased, the measured resistance decreased, which was expected. The inverse relationship between measurement temperature and sample resistance stems from the mobility of ions at different temperatures. As the temperature increases, the ionic mobility increases and the ion is able to move through the sample more freely. This relationship was illustrated

using the Arrhenius equation earlier (Equation 9). In this equation, conductivity is related to temperature, where an increase in temperature causes an increase in ionic conductivity and therefore a decrease in resistivity and resistance, as shown in Figure 15.

To determine the effects of contact resistance over a range of temperatures, linear trend lines were fit to resistance values of samples with different thicknesses measured at a specific temperature. This was done for all temperatures in the temperature range, so that each temperature had its own corresponding data set. The extrapolation of these trend lines gave the resistance for a sample with zero thickness at that specific temperature. This value (y-intercept for trend line) was determined to be the contact resistance for that sample set at that given temperature. Calculating the intercept for all temperatures at which the samples were measured allowed for the evaluation of temperature effects on contact resistance for the different electrode materials under these conditions. Figure 16 shows the plots of contact resistance as a function of temperature and electrode material.

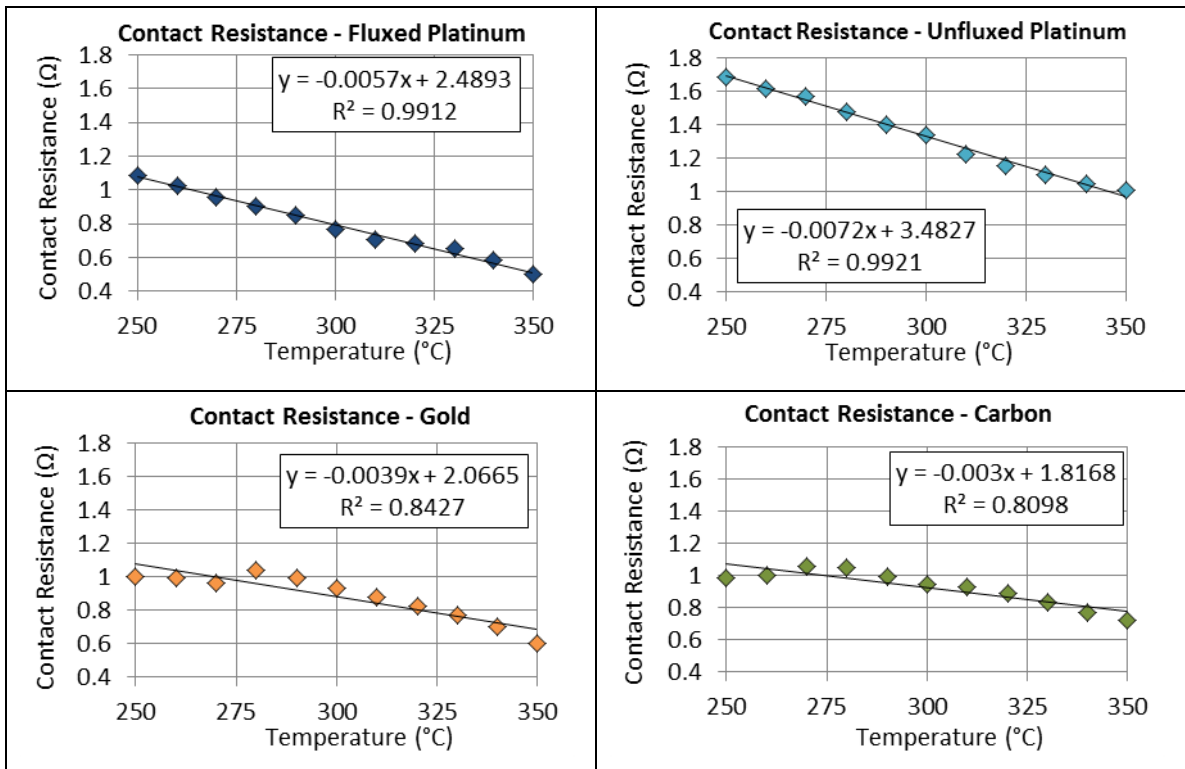


Figure 16. Contact resistance as a function of temperature measured using four different electrode materials.

It was observed that contact resistance for all four electrode materials varied with measurement temperature. Contact resistance values for both fluxed and unfluxed platinum appeared to be mainly linear, where contact resistance decreased as temperature increased. However, the slopes for the two platinum electrodes were not the same. Unfluxed platinum had a slightly steeper slope and greater contact resistance over the entire temperature range compared to that of fluxed platinum. Contact resistance plots for gold and carbon electrodes were less definitive. Both materials appeared to have linear trends for contact resistance at temperatures above 280 °C; however, that trend was not observed at lower temperatures. There, constant contact resistance values were observed. The cause of this trend is not understood. For these two electrode materials, contact resistance is constant at lower temperatures until a threshold temperature (roughly 280 °C), at which point contact resistance decreased linearly with increased temperature.

Quantifying contact resistance in the different electrode scenarios allowed for the data to be corrected accordingly. The results are seen below in Figure 17.

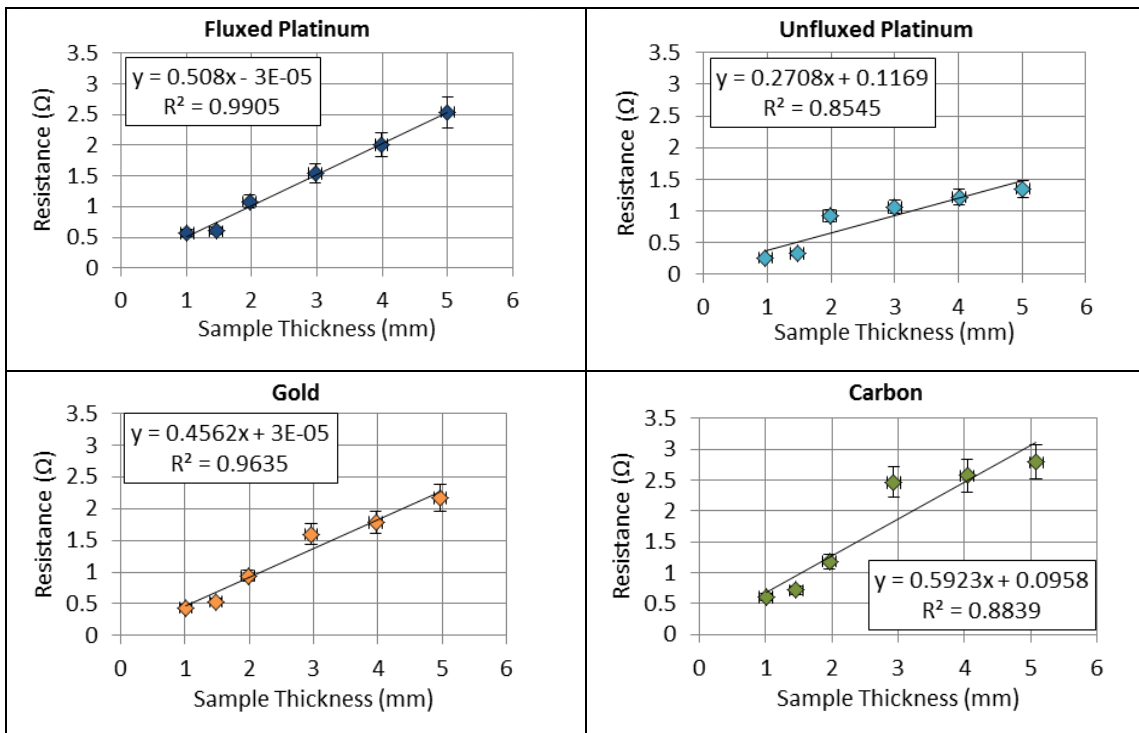


Figure 17. Sample resistance with respect to thickness for samples measured with different electrode materials. Data has been corrected to exclude contact resistance. Linear trend lines were fit to the data with varying success (see text).

Subtracting contact resistance from measured resistance allowed for the determination of pure sample resistance. The corrected data were plotted with respect to sample thickness for each of the electrode materials. A linear trend was observed and a trend line was fit to this data. It was expected that after the data were corrected and the contributions of contact resistance subtracted, resistance of a sample with zero thickness would be zero ohms. This principal was observed in both the fluxed platinum and gold electrode data, but not the unfluxed and carbon electrode data. This was attributed to variation in data from outlying points (2 mm unfluxed platinum and 3 mm carbon) with error bars that did not intersect the data's trend line. Had these outlying points not been included in trend line fitting, the y-intercept for the unfluxed platinum and carbon data would have been much closer to zero. Resistance was plotted on identical axes for all four materials to illustrate the differences in resistance values. Samples with small thickness (1 mm) had similar resistance for all four electrode materials; however, the slopes of the data differed, which indicated variation between electrode materials.

Examining sample resistance was very useful, particularly for determining the amount of contact resistance in the samples. However, when comparing electrical performance of materials it is usually beneficial to examine values linked to material properties and not just measured values. One such example is resistivity. Resistivity is obtained using Equation 7 with the measured values of resistance, electrode area and sample thickness. It is conveyed as the amount of resistance times a length component, usually cm, that is obtained from quantity A/L , and is expressed in units of Ohms•cm. Figure 18 shows the resistivity of measured samples with respect to sample thickness for all four electrode materials.

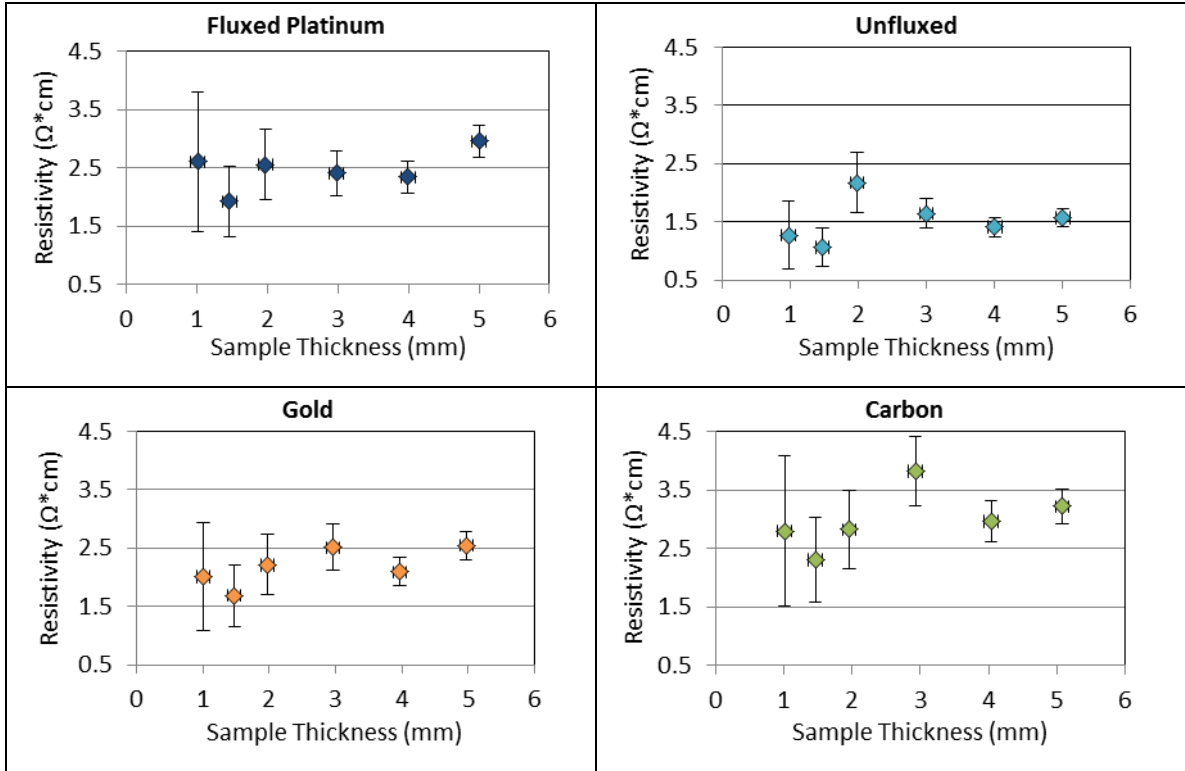


Figure 18. Resistivity vs. sample thickness at 300 °C for samples measured using four different electrode materials. (Corrected to account for contact resistance).

Sample data were graphed on identical axes to compare data more effectively. Sample error bars range from 9.4% to 46%, increasing as sample thickness decreased, using the following equation.

$$d\rho = dR\left(\frac{A}{L}\right) + dA\left(\frac{R}{L}\right) - dl\left(\frac{RA}{L^2}\right) \quad (11)$$

$d\rho$ = Uncertainty in resistivity

dR = Uncertainty in resistance

dA = Uncertainty in area measurement

dL = Uncertainty in thickness measurement

A = electrode area (cm²)

L = sample thickness (cm)

The fluctuation in A/L caused the overall error in resistivity data to vary depending on sample thickness. Although sample thickness affected the error associated with resistivity data, it was observed that the resistivity reported for each electrode material was relatively consistent regardless of sample thickness. This was promising as we would not expect resistivity to vary depending on which type of electrode material was used, nor would we expect for the resistivity to change with sample thickness. Resistivity is a material property; therefore it should stay constant regardless of sample thickness and electrode used. Determining whether the different electrode materials produced similar results for the same sample was another matter entirely. A direct comparison of sample resistivity for all four electrodes is shown in Figure 19. Additionally, Table IX shows the average resistivity value and activation energy for all four electrode configurations.

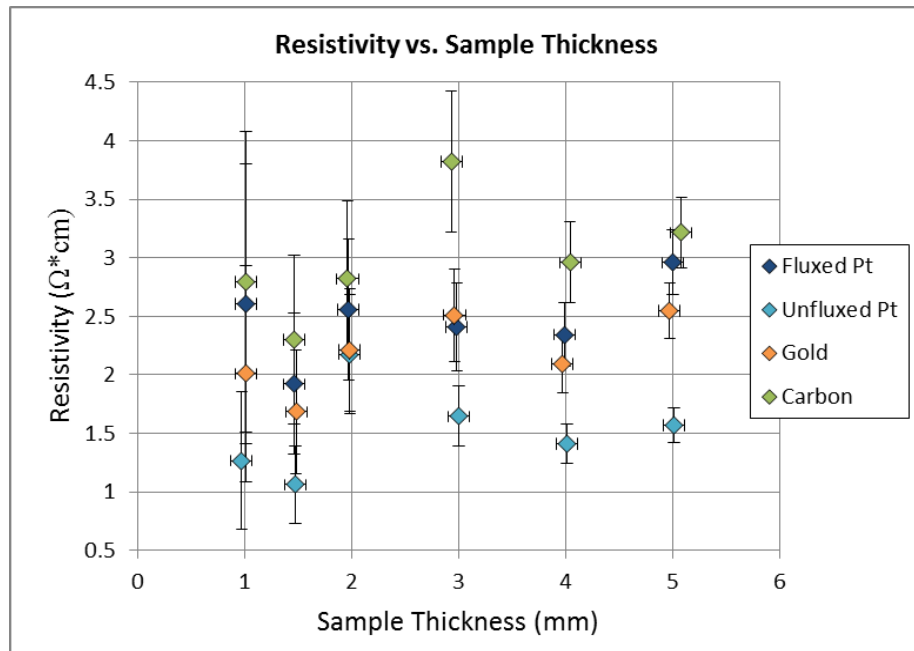


Figure 19. Resistivity vs. sample thickness at 300 °C for four different electrode materials used to measure the same samples.

Although much of the data overlapped, there were some visible trends. First, data obtained using unfluxed platinum electrodes were consistently lower than that of other electrodes. Gold and fluxed platinum data were fairly similar, while carbon data gave the

highest values of resistivity overall. Table IX shows the average resistivity and activation energy for all four electrode materials, tabulate below.

Table IX. Measured Sample Resistivity and Activation Energy for Samples Measured Using Four Different Electrode Materials

	Average Sample Resistivity ($\Omega \cdot \text{cm}$)	Average Activation Energy (eV)
Fluxed Platinum	2.5 +/- 0.4	0.15 +/- 0.02
Unfluxed Platinum	1.5 +/- 0.2	0.15 +/- 0.02
Gold	2.2 +/- 0.3	0.15 +/- 0.02
Carbon	3.0 +/- 0.5	0.20 +/- 0.02

Tabular data highlights the differences between data collected using different electrode materials. It was observed that the two materials which gave the closest results for sample resistivity were fluxed platinum and gold. Additionally these two materials gave relatively similar results for activation energy. Results for activation energy of samples measured using different electrodes are seen in Figure 20.

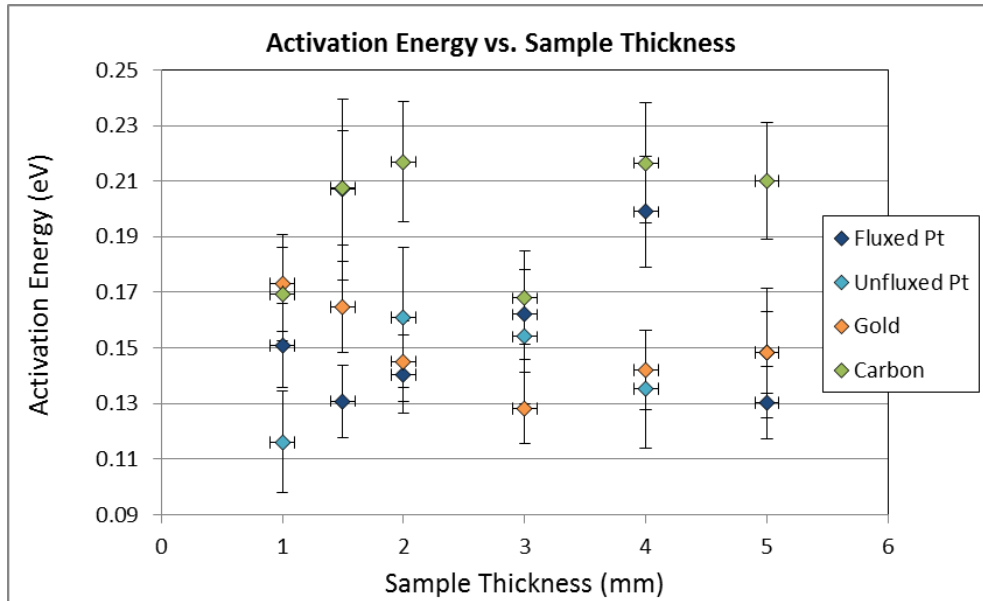


Figure 20. Activation energy vs. sample thickness for different electrode materials used to measure the same sample sets.

Activation energy was obtained using Arrhenius plots of $1/T$ vs. $\ln(\rho/T)$, where the slope of the data plotted in this manner provided a means for calculating activation

energy. It was observed that fluxed platinum, unfluxed platinum and gold electrode setups all gave similar values for activation energy independent of sample thickness. Samples measured using carbon electrodes recorded sample activation energies higher than then those of other electrode materials.

B. Excess Soda Studies

1. Composition

The second main objective of this study was to quantify the effects of slight composition variation on the electrical properties of β'' -alumina. The processing of beta alumina is somewhat difficult. Excess sodium is often introduced to counteract soda loss during processing and sintering. However, too much excess sodium is not favorable as it can encourage the formation of a secondary phase which can negatively affect mechanical stability of the sintered product. To evaluate the effect of excess sodium on the electrical properties of sintered samples, two compositions were carefully selected. The ideal composition for zinc stabilized β'' -alumina is given in Table X. Composition targets for the two excess soda compositions selected for this study are shown in Table XI and Table XII.

Table X. Composition Targets for Ideal Zinc Doped Composition
($\text{Na}_{1.67}\text{Zn}_{0.67}\text{Al}_{10.33}\text{O}_{17}$)

	Mole %	Weight %		
Al_2O_3	77.5	82.259	Na/Al	0.161
Na_2O	12.5	8.163	Zn/Al	0.064
ZnO	10	8.578	Na/Al excess	0

Table XI. Composition Targets for Z3 Powder (Excess Na/Al =0.01)

	Mole %	Weight %		
Al_2O_3	76.953	82.890	Na/Al	0.172
Na_2O	13.207	8.647	Zn/Al	0.064
ZnO	9.841	8.463	Na/Al excess	0.010

Table XII. Composition Targets for Z4 Powder (Excess Na/Al = 0.02)

	Mole %	Weight %		
Al ₂ O ₃	76.317	82.425	Na/Al	0.181
Na ₂ O	13.836	9.084	Zn/Al	0.065
ZnO	9.847	8.491	Na/Al excess	0.020

Z3 and Z4 compositions were selected to introduce excess soda into the base composition of the beta alumina without changing the base structure. This was done by altering the molar ratio of Na to Al, but not the ratio of Zn to Al. The ideal ratio of sodium to aluminum for β'-alumina is 0.161. This ratio was increased by 0.01 initially to produce the Z3 composition. This Z3 composition introduced a small amount of excess sodium into the batch, which increased the final sodium content after production. The composition developed to integrate a larger amount of excess soda into the base unit was the Z4 composition. This composition provided excess sodium at a ratio excess of 0.02 Na/Al. Compositional effects on processing can often be realized during powder processing. Figure 21 shows SEM images of spray dry granules for Z3 and Z4 compositions respectively.

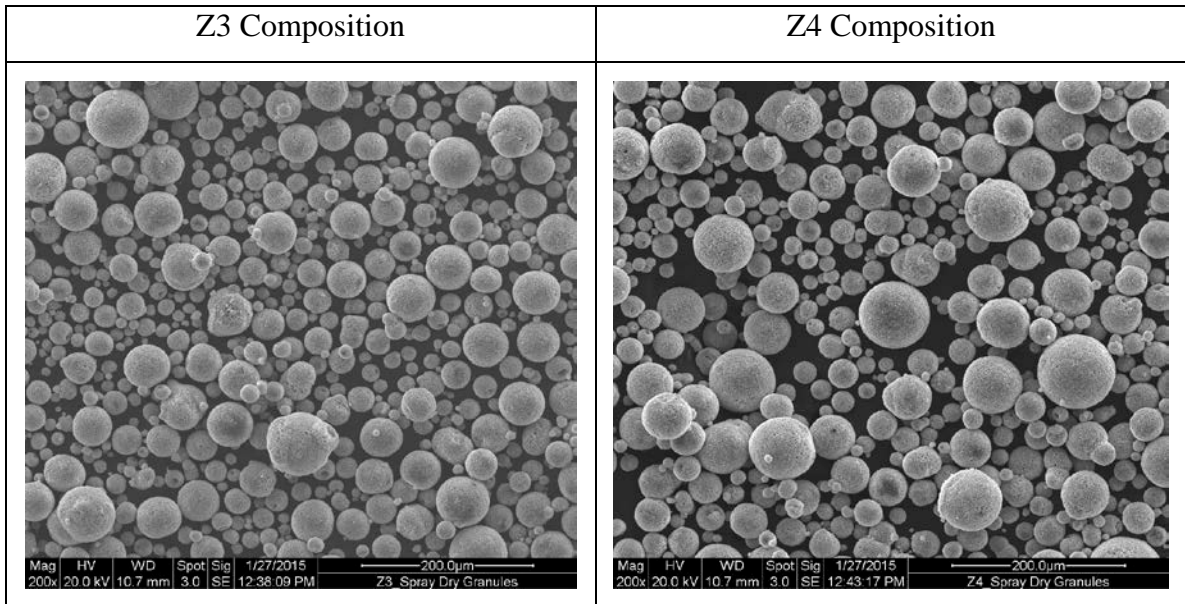


Figure 21. Spray dried granules for Z3 and Z4 compositions.

Compositional effects on spray dry granule size for the two batches are seen in the images above. Image processing software allowed for the measurement of average granule size. Z3 compositions had an average granule size of 22.4 μm , while the Z4 composition had an average granule size of 25.1 μm . This 10% difference in average granule size did not have noticeable effects on the sintered samples.

2. Material Properties

a. Density (Effect of Sintering and Composition on Density)

Sintered sample density and percent theoretical density are displayed in Tables XIII and XIV. Table XIII contains density data for samples sintered from Z3 powder; the composition which contained the least amount of excess sodium ($\text{Na/Al excess} = 0.01$). Table XIV contains density data for samples sintered from Z4 powder; the composition which contained the most excess sodium ($\text{Na/Al} = 0.02$).

Table XIII. Density of Sintered Pellets Pressed from Composition Z3 Powder

Theoretical Density = 3.382			
Temperature ($^{\circ}\text{C}$)	Time	Density	% Theoretical
1610	30 min	3.068	90.70
1625	30 min	3.287	97.17
1640	30 min	3.305	97.73

Temperature ($^{\circ}\text{C}$)	Time	Density	% Theoretical
1610	1 hour	3.178	93.98
1625	1 hour	3.296	97.47
1640	1 hour	3.297	97.47

Table XIV. Density of Sintered Pellets Pressed from Composition Z4 Powder

Theoretical Density =3.400

Temperature (°C)	Time	Density	% Theoretical
1610	30 min	3.137	92.26
1625	30 min	3.306	97.23
1640	30 min	3.310	97.34

Temperature (°C)	Time	Density	% Theoretical
1610	1 hour	3.161	92.95
1625	1 hour	3.317	97.53
1640	1 hour	3.301	97.06

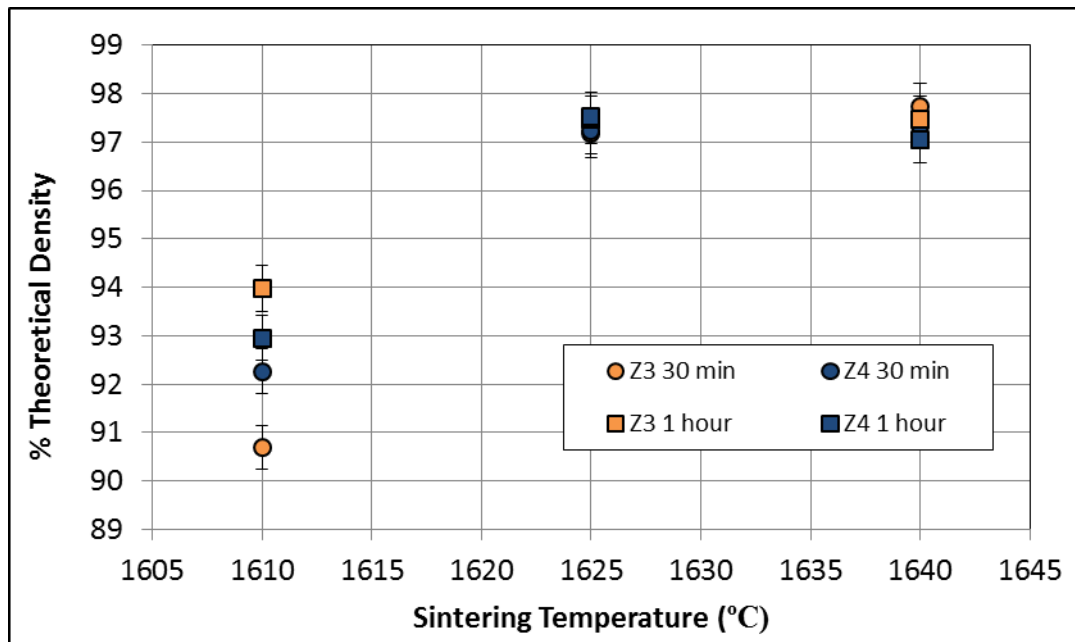


Figure 22. Effect of sintering temperature on percent theoretical density of sintered samples.

Figure 22 shows sample densification for sintered samples of both Z3 and Z4 compositions, shown as percent theoretical density as a function of sintering temperature. Samples made from Z3 powders are represented by orange data points while Z4 samples are represented in blue. Data symbol shapes indicate the two different dwell times during sintering: 30 minutes and 1 hour.

It was observed that at the lowest sintering temperature (1610 °C), samples densified to 90-94% of theoretical density. The densification in this range did not appear to be a result of the sample's composition. However, it was observed that both compositions sintered to slightly higher densities at a 1 hour dwell time. Samples with an increased sintering temperature of 1625 °C showed increased densification to 97-98% theoretical density. There appeared to be no effect of sample composition or sintering time on densification of the samples at that temperature; all samples densified to roughly the same percent theoretical density. Further increasing sintering temperature did not affect the overall densification of the sintered samples. Samples sintered at 1640 °C also densified to between 97 and 98% of theoretical density. Again, densification appeared to be independent of sample composition and sintering time.

b. Microstructure and Grain Size (Effect of Sintering and Composition on Grain Size)

The microstructures of sintered samples were investigated to evaluate grain growth as a function of sintering temperature, sintering time and composition. Figure 23 shows the effect of sintering time and temperature on both compositions. It was observed that increased sintering temperatures and sintering times lead to increased grain growth, resulting in larger average grain size. This is illustrated by the images in Figure 23. As time and temperature were increased, smaller grains began to coalesce, and form larger grains with more developed microstructures.

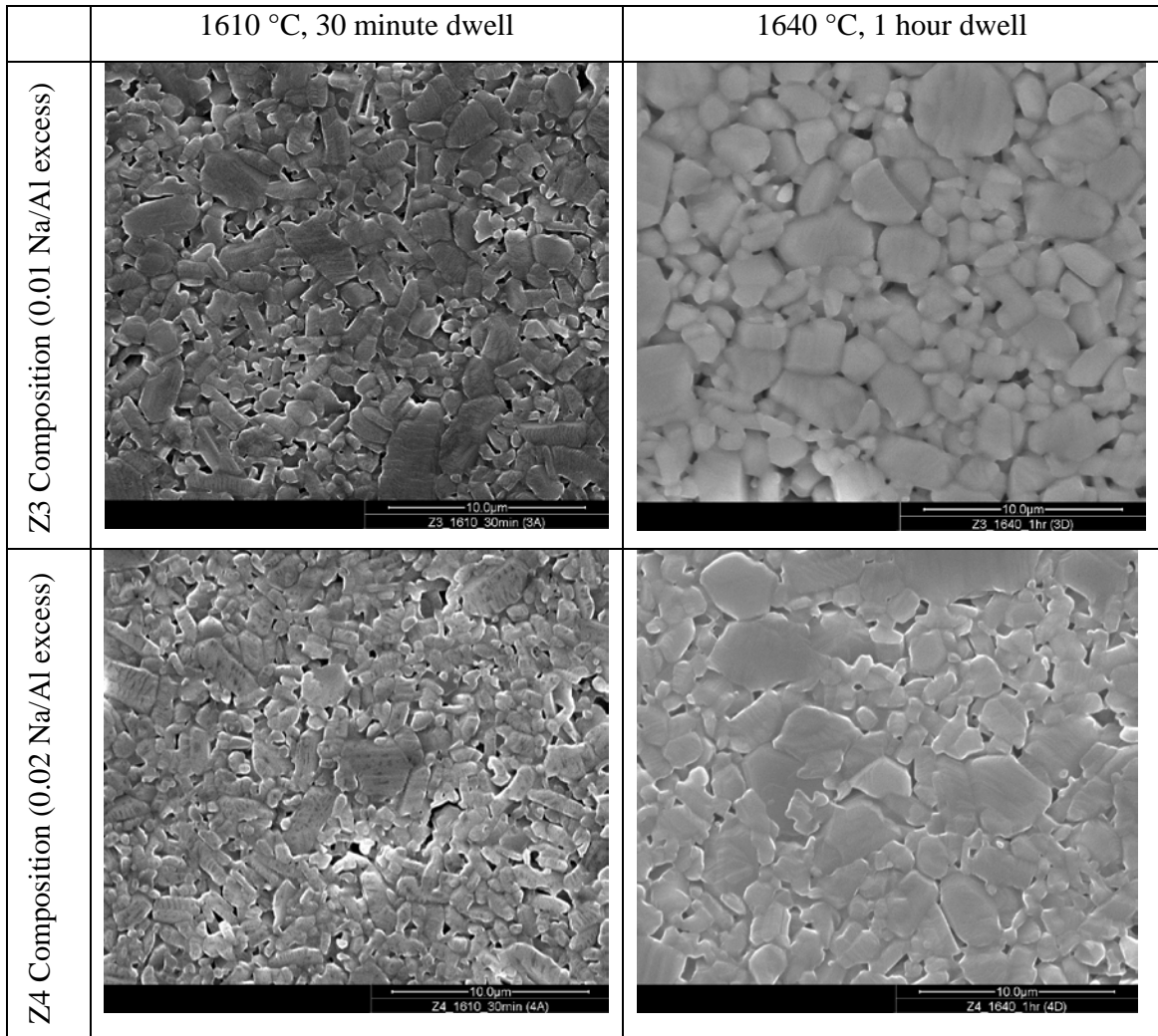


Figure 23. Photomicrographs Show Samples of Z3 and Z4 Compositions Sintered to Different Conditions Producing Different Average Grain Sizes.

As grain growth occurs in a ceramic body, smaller grains begin to grow together to form larger grains with more developed microstructures. This grain growth is affected by both sintering temperature and dwell time. Generally, the higher the sintering temperature, the more grain growth will occur. This is due to an increase in transport between grains at higher temperatures. The same is also generally true for sintering time. As sintering time is increased, grain size generally also increases. The longer the sample is held at the sintering temperature, the more time there is for small grains to consolidate and develop into larger grains. This behavior is observed when examining average measured grain size for samples from each data set in the sample matrix. Table XV

shows the average grain size for samples of each composition sintered at a variety of sintering temperatures and times.

Table XV. Average Measured Grain Sizes for Sintered Samples

Composition Z3

	1610 °C	1625 °C	1640 °C
30 min	0.94 ± 0.02	1.18 ± 0.07	1.34 ± 0.04
1 hour	1.03 ± 0.04	1.26 ± 0.11	1.54 ± 0.02

Composition Z4

	1610 °C	1625 °C	1640 °C
30 min	0.89 ± 0.01	1.04 ± 0.07	1.23 ± 0.03
1 hour	0.97 ± 0.04	1.17 ± 0.10	1.39 ± 0.05

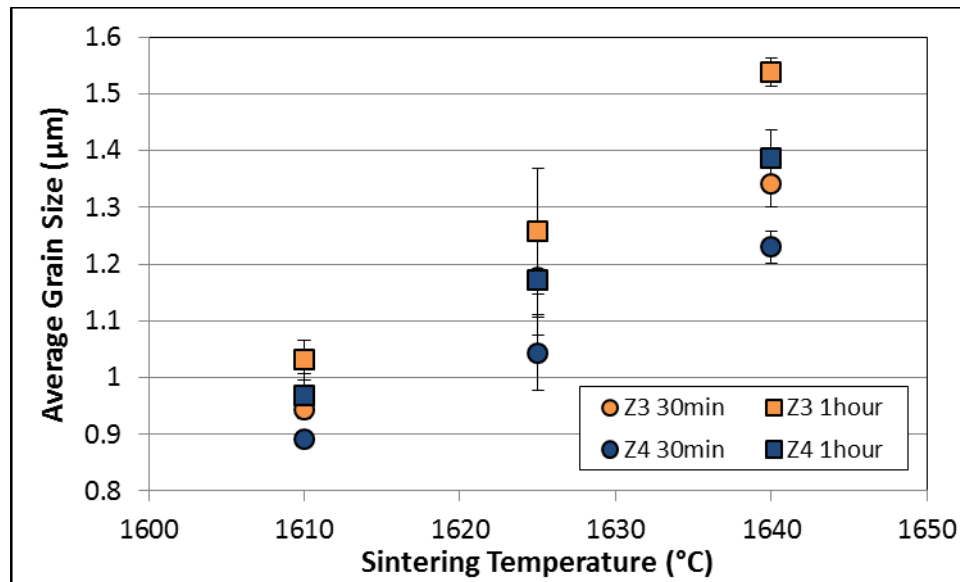


Figure 24. Effect of sintering time, temperature and composition on average grain size.

Figure 24 shows the effect of sintering time and temperature on average grain size. Samples of Z3 composition are shown in orange and Z4 compositions are shown in blue. Marker shape indicated the difference in sample sintering times. Error bars show the range of grain sizes measured from the three microstructures taken for each sample. It

was observed that average grain size increased as sintering temperature increased, for each sintered sample set. Additionally, samples sintered for the longer sintering time of 1 hour sintered to larger grain size than their 30 minute counterparts. Overall, it was seen that samples comprised of the Z3 composition (0.01 Na/Al excess) sintered to larger grain sizes than samples of Z4 composition (0.02 Na/Al excess). The role of excess sodium as a sintering aid in β'' -alumina was also examined. Samples made with the most excess sodium in the composition sintered to smaller grain sizes overall, indicating that excess sodium in the material did not act as a sintering aid.

The ternary phase diagram for the Na_2O - MgO - Al_2O_3 system shows that in excess Na_2O in the β'' -alumina system leads to the formation of sodium aluminate (NaAlO_2).²⁷ It is possible that excess soda not incorporated into the β'' -alumina structure migrated to the grain boundary during sintering. Once at the grain boundary, the excess soda would have formed a sodium aluminate phase which could have inhibited grain growth. The amount of sodium aluminate at the grain boundary would likely have been affected by the overall level of excess soda in the composition. If this were the case, the composition with more excess soda would likely form more sodium aluminate at the grain boundary, which would in turn retard the sintering process and inhibit larger grains from forming. Quantifying grain size for each sample set was important for the comparison of impedance data on the basis of grain size, since it was speculated that grain size played an important role on ionic conductivity of ceramic materials.

c. XRD

X-Ray diffraction was performed to confirm that the desired phase of Na β'' -alumina was obtained, and to investigate the presence of the secondary sodium aluminate phase. Although this phase may only exist in small quantities, it was possible that the diffraction pattern would show small peaks that could be attributed to sodium aluminate.

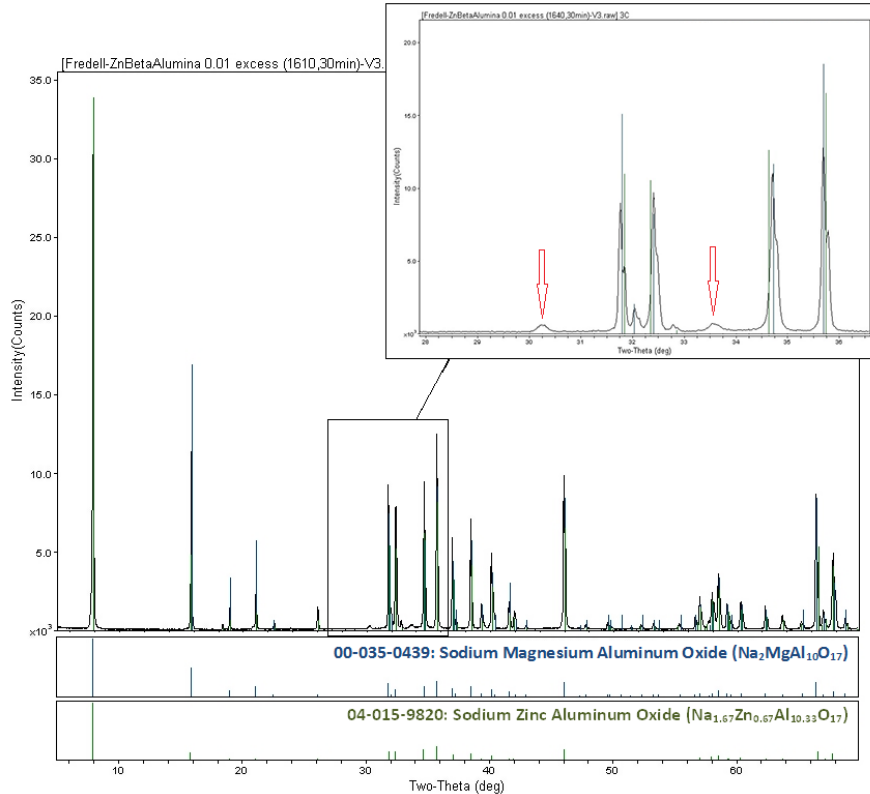


Figure 25. XRD pattern for a sintered sample of zinc doped β'' -alumina identified and matched with corresponding XRD cards for the primary phase.

Figure 25 shows the XRD pattern collected for a sample sintered from Z3 composition at 1610 °C for 30 minutes. This sample provides a representative pattern, as the difference among the patterns of the sintered samples was observed to be very slight. Using Jade software, the pattern was matched to PDF cards from the diffraction database. The experimental patterns showed a good match to two closely related PDF patterns; a sodium magnesium aluminum oxide ($\text{Na}_2\text{MgAl}_{10}\text{O}_{17}$) and sodium zinc aluminum oxide ($\text{Na}_{1.67}\text{Zn}_{0.67}\text{Al}_{10.33}\text{O}_{17}$). The sodium magnesium aluminum oxide represents the perfect stoichiometric phase of magnesium doped β'' -alumina. In this research, the β'' -alumina structure was stabilized using zinc (Zn^{2+}) ions instead of magnesium (Mg^{2+}) ions, so this pattern can be related to the equivalent zinc stabilized phase ($\text{Na}_2[\text{Zn}]\text{Al}_{10}\text{O}_{17}$). This allowed for this PDF card to be used for identification based on its structural attributes regardless of the fact that it used a different stabilizing ion. The second pattern was a zinc-stabilized β'' -alumina. This phase had a slightly different stoichiometry than

prepared in this study. The stick patterns for both phases can be seen below the experimentally obtained pattern.

Although these patterns matched the XRD data very well, Figure 25 highlights two smaller peaks that were not present in the reference patterns. These smaller peaks were located at roughly 30 and 33.5 °2θ. According to previous literature, the presence of a secondary sodium aluminate phase is common when synthesizing and sintering β''-alumina material.^{19, 28, 46} Therefore, it was assumed that these two unidentified peaks could be attributed to the presence of another phase formed during processing or sintering. Again, Jade software was used to match these peaks to a pattern from the diffraction database.

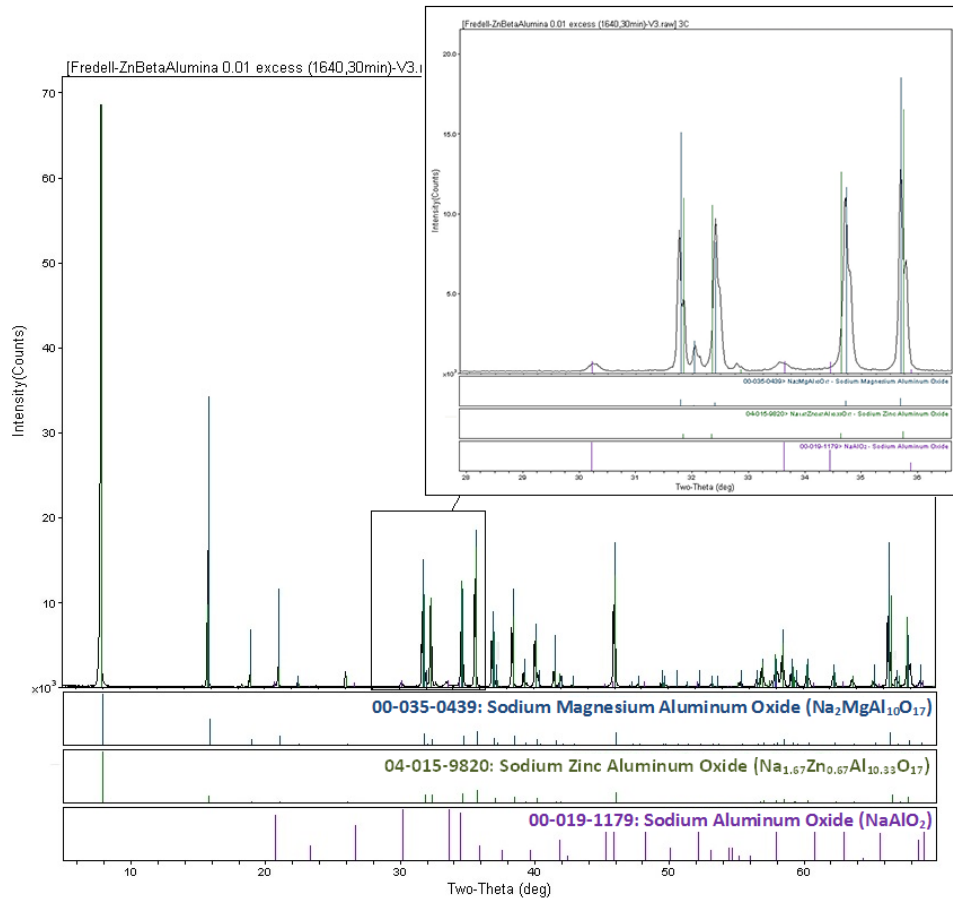


Figure 26. XRD pattern of sintered zinc doped β''-alumina. The primary phase is identified as well as the minor secondary phase (NaAlO₂).

Figure 26 shows the experimental diffraction pattern with PDF card patterns from the diffraction database. The two PDF cards that fit the primary phase are shown in blue and green. The third stick pattern shown in purple is for the secondary sodium aluminate phase. This PDF showed peaks that fit the two unidentified peaks and overlapped with other peaks in the pattern. This helped confirm the presence of a secondary phase in the material. Relative peak intensity indicated that only a small amount of this secondary phase was present. To try and quantify the amount of this secondary phase, x-ray patterns were collected for samples of each sintering parameter and composition. Patterns for sintered Z3 samples are seen in Figure 27. Figure 28 shows the diffraction patterns for sintered Z4 samples.

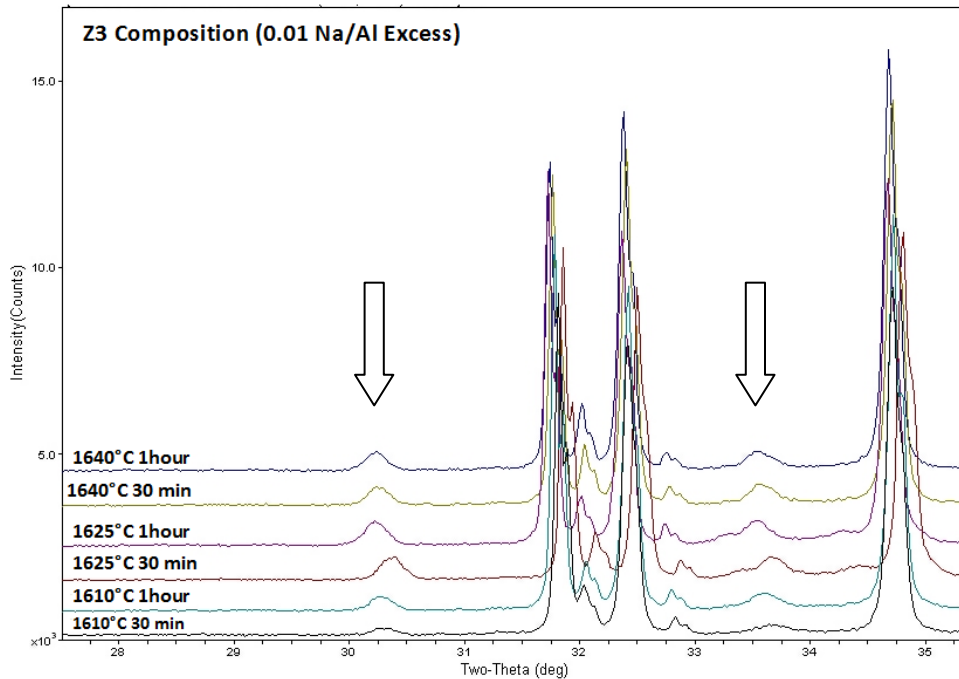


Figure 27. XRD patterns for composition Z3 samples comparing the relative size of the two main peaks for the secondary phase (NaAlO_2) between sintering conditions.

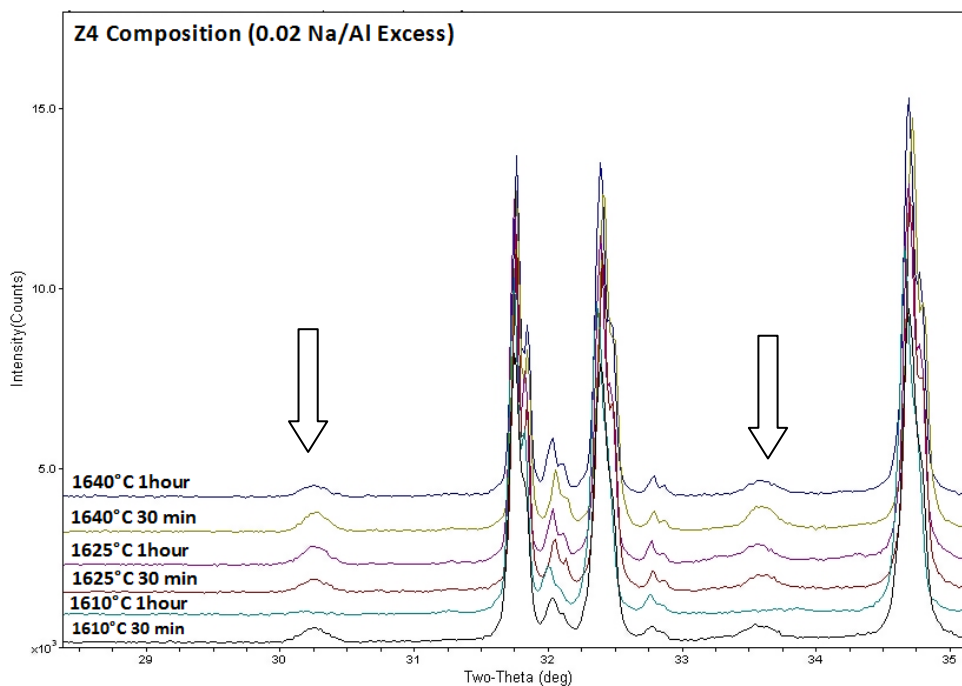


Figure 28. XRD patterns for composition Z4 samples comparing the relative size of the two main peaks for the secondary phase (NaAlO_2) between sintering conditions.

Figure 27 and Figure 28 compare XRD patterns for samples sintered at a variety of parameters for both Z3 and Z4 compositions. To quantify the subtle variation in peaks, Jade software was used to calculate peak area. This process was accomplished by fitting a profile to the patterns and identifying peaks. Next, relative peak area was determined by comparing the area of the smaller peaks to that of the largest peak of the primary β'' -alumina phase.

Table XVI shows the peak area for all sintered sample patterns for both sodium aluminate peaks (30° & $33.5^\circ 2\theta$). Data was graphed to help illustrate the trends in peak area. Figure 29 shows the effect of composition and sintering parameters on peak area for the two sodium aluminate peaks. It was observed that for the Z3 samples, the largest peak area appeared for samples sintered at the median sintering temperature of 1625°C and was smaller at the higher temperature of 1640°C . However, the same trend was not seen in the Z4 composition samples.

Table XVI. Peak Areas of Secondary Phase (NaAlO_2) for all Sintered Samples of Both Compositions

Composition	Sintering Conditions	First Peak Location ($^{\circ}2\theta$)	Peak Area (%)	Second Peak Location ($^{\circ}2\theta$)	Peak Area (%)
Z3	1610 $^{\circ}\text{C}$ 30min	30.29	1.6	33.67	3.6
Z3	1625 $^{\circ}\text{C}$ 30min	30.36	5.3	33.66	7.0
Z3	1640 $^{\circ}\text{C}$ 30min	30.24	2.1	33.57	3.1
Z3	1610 $^{\circ}\text{C}$ 1 hour	30.27	2.6	33.60	4.4
Z3	1625 $^{\circ}\text{C}$ 1hour	30.22	4.1	33.53	4.3
Z3	1640 $^{\circ}\text{C}$ 1hour	30.22	1.7	33.55	2.5
Z4	1610 $^{\circ}\text{C}$ 30min	30.24	2.5	33.56	4.1
Z4	1625 $^{\circ}\text{C}$ 30min	30.24	2.3	33.59	3.6
Z4	1640 $^{\circ}\text{C}$ 30min	30.25	2.2	33.58	4
Z4	1610 $^{\circ}\text{C}$ 1 hour	30.17	0.3	33.74	1.4
Z4	1625 $^{\circ}\text{C}$ 1hour	30.25	3.0	33.51	3.5
Z4	1640 $^{\circ}\text{C}$ 1hour	30.24	1.6	33.59	3.0

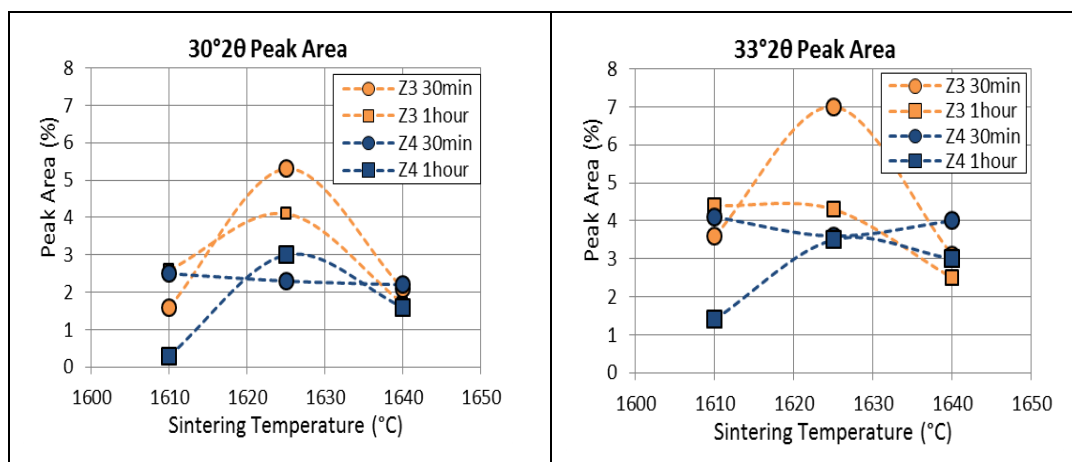


Figure 29. Peak area for the two main sodium aluminate peaks (roughly 30 and 33 $^{\circ}2\theta$).

There are several scenarios to consider when interpreting the data. It can be speculated that the samples sintered to the lowest temperature would have the most sodium aluminate because they would have the least amount of sodium loss and therefore the most remaining sodium to convert to sodium aluminate. Conversely, it could be argued that higher temperatures help encourage the formation of sodium aluminate at the grain boundaries and therefore samples sintered to the highest temperatures would contain the most amount of this secondary phase. However, neither of these hypotheses

could be substantiated as there was no discernable, or consistent, trend in the data. It would certainly be expected that the Z4 composition would have a higher sodium aluminate peak area due of the larger amount of excess sodium in the composition. This was not shown in the collected data. Overall, it was not possible to quantitatively determine the relative amount of the secondary phase in these samples. No conclusions regarding the effects of composition or sintering temperature on the amount of sodium aluminate was obtained from these data; only the positive identification of the phases present in the sintered materials could be made.

Figure 30 shows the fitting of the two sodium aluminate peaks using an offset of zero. Jade software refined the data and used the Scherrer equation to determine the crystallite size of the material. It was determined that crystallite size of the sodium aluminate material was between 400 nm and 600 nm. The size of these grains is smaller than the average grain size of the β'' -alumina.

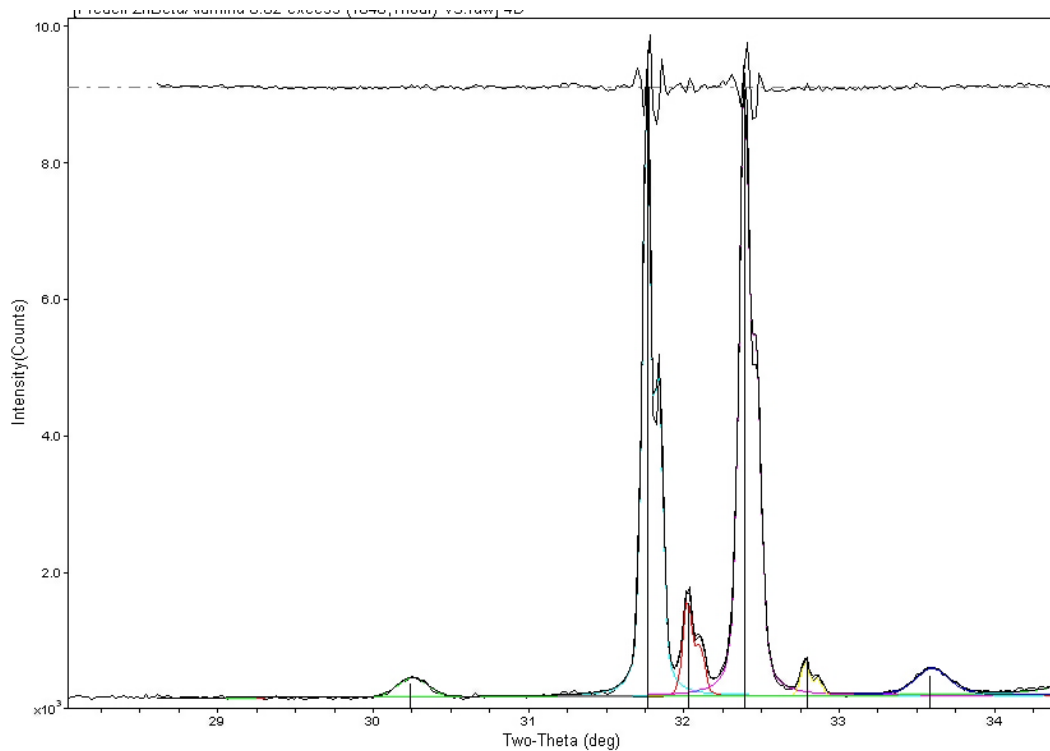


Figure 30. Calculation of crystallite size for 30 °2θ and 33 °2θ using peak fitting and the Scherrer Equation.

d. ICP

ICP analysis was performed on synthesized Na β'' -alumina powders of both Z3 and Z4 compositions, as well as on sintered samples of each composition. One sample from each sintering condition and composition was ground into a powder and tested using ICP MS analysis. Z3 composition data were shown in orange while Z4 composition data were shown in blue. Again, different data point shapes represent different sintering times.

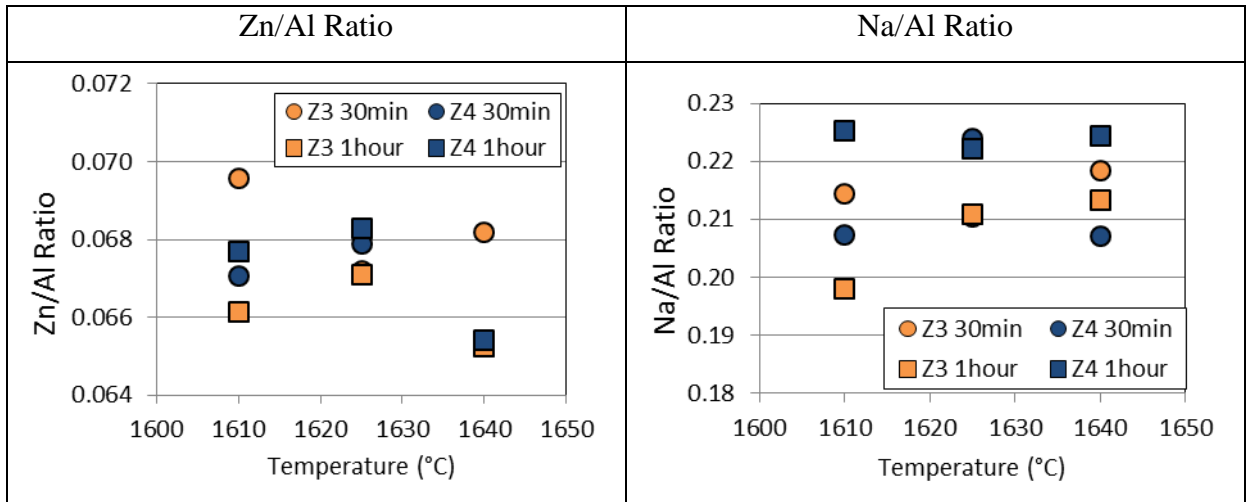


Figure 31. Effect of sintering time and temperature on Zn/Al and Na/Al ratios.

The effect of time, temperature and composition on Zn/Al and Na/Al ratios is shown in Figure 31. It is observed that sintering time and temperature did not have any distinct effect on either Zn/Al or Na/Al ratios.

Table XVII. ICP Analysis of Zn/Al and Na/Al Molar Ratios in Powders and Samples

	Zn/Al	Na/Al
Ideal Composition	0.065	0.161
Z3 Target	0.064	0.172
Z3 Powder Unsintered	0.067	0.211
Z3 Sintered Samples	0.067	0.214
Z4 Target	0.065	0.181
Z4 Powder Unsintered	0.067	0.218
Z4 Sintered Samples	0.067	0.223

Although Zn/Al and Na/Al ratios were independent of sintering time and temperature, some effect of composition type was observed. Table XVII shows the molar ratio targets for the ideal Zn β'' -alumina composition as well as the two sodium excess compositions synthesized during this work. The goal was to hold Zn/Al ratios constant for all materials, while varying Na/Al ratios slightly depending on the composition. It was observed that Zn/Al ratios were slightly higher than the composition targets for Z3 and Z4 materials, but that they were consistent between the two compositions. Na/Al ratios for both Z3 and Z4 compositions were higher than the targeted value, 0.21 and 0.22, respectively, as opposed to the composition targets of 0.17 and 0.18 Na/Al. This indicated that more sodium than intended was present in the system; 0.05 and 0.06 Na/Al excess respectively. Although there was slightly more sodium in each composition than predicted, there was still the same difference in Na/Al ratio between the two compositions, with the Z4 composition having 0.01 more excess Na/Al than the Z3 composition. Although the compositions were slightly different than expected, it still allowed for the evaluation of varying levels of excess sodium in the β'' -alumina system on densification and ionic resistivity. Additionally, when comparing composition targets of unsintered and sintered materials, it was observed that Zn/Al and Na/Al ratios remained consistent regardless of sintering. This shows that little or no sodium was lost during the sintering process, indicating that the precautions used to mitigate sodium loss were effective.

3. Electrical Properties

Impedance spectroscopy was performed to determine the electrical properties of the different sintered samples. For these samples, fluxed platinum electrode paste and solid platinum electrodes were used. Impedance spectroscopy data were analyzed to determine sample resistance.

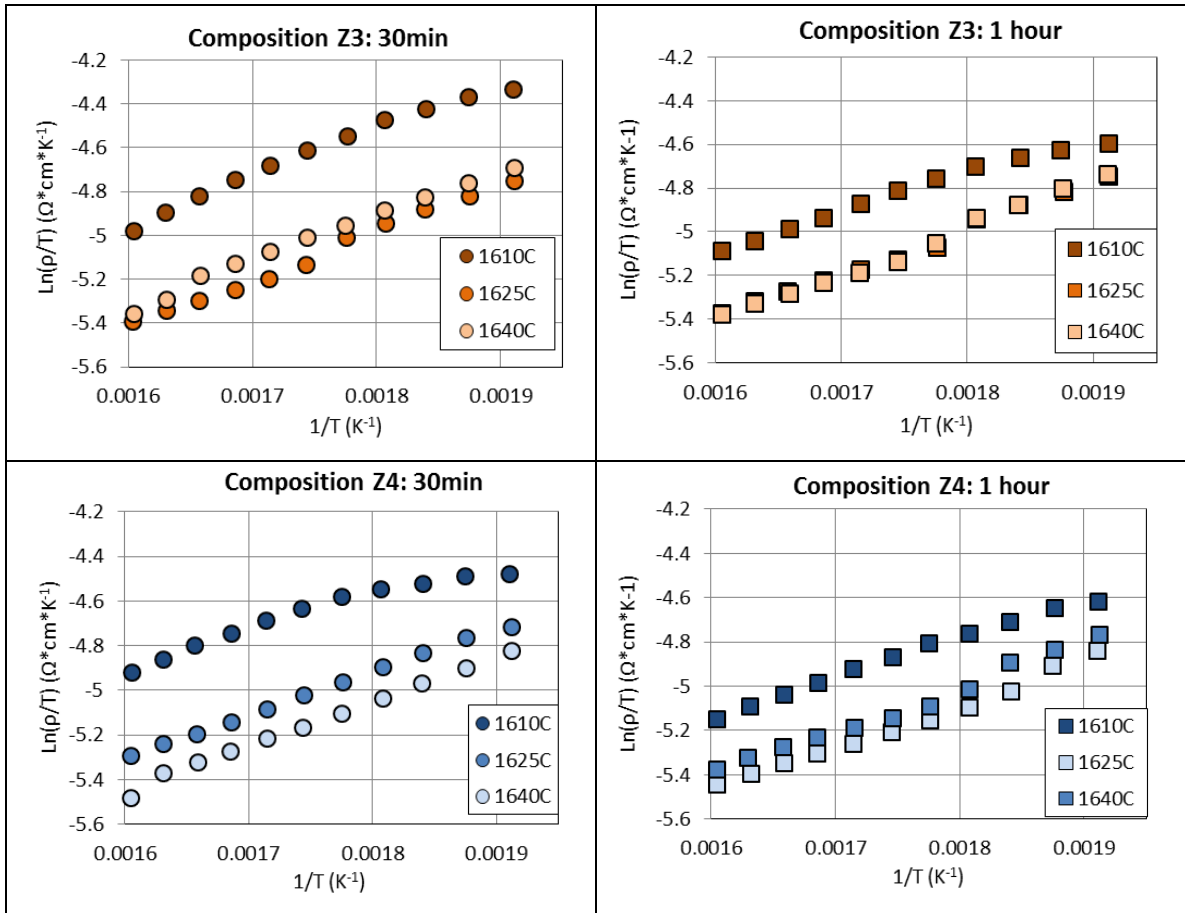


Figure 32. Arrhenius plots for sintered samples of both Z3 and Z4 compositions over a variety of sintering temperatures and sintering times.

Figure 32 shows Arrhenius plots for Z3 and Z4 samples sintered for 30 minutes and 1 hour. Data shown in orange correspond to Z3 composition while blue data correspond to Z4 composition data. Sintering times are differentiated by symbol shape, with circles representing 30 minute data and squares representing 1 hour data. Plotting data in Arrhenius plots allowed for the calculation of activation energy for each sample. The Arrhenius plot showed several trends. It was observed that the data were generally

linear when plotted in Arrhenius format and also that data sets were separated by sintering temperatures. The linear trend of the data is favorable as it indicates the presence of a single conduction mechanism in the material. In all cases, samples with the lowest sintering temperatures had the highest resistivity values. This was attributed to an increase in density and grain size for the samples sintered at increased temperatures. Samples sintered at 1625 °C and 1640 °C had smaller resistivity values than samples sintered at 1610 °C. These values were either slightly separated or near overlapping depending on the sintering time and composition. Samples of Z3 and Z4 compositions sintered to 1 hour had very close 1625 °C and 1640 °C data compared to that of samples sintered to 30 minutes. This slight variation was attributed to the difference in grain size that resulted from prolonged sintering times.

Figure 33 and Figure 34 show the effect of temperature on resistivity for a variety of samples sintered at different sintering specifications for the Z3 and Z4 powders.

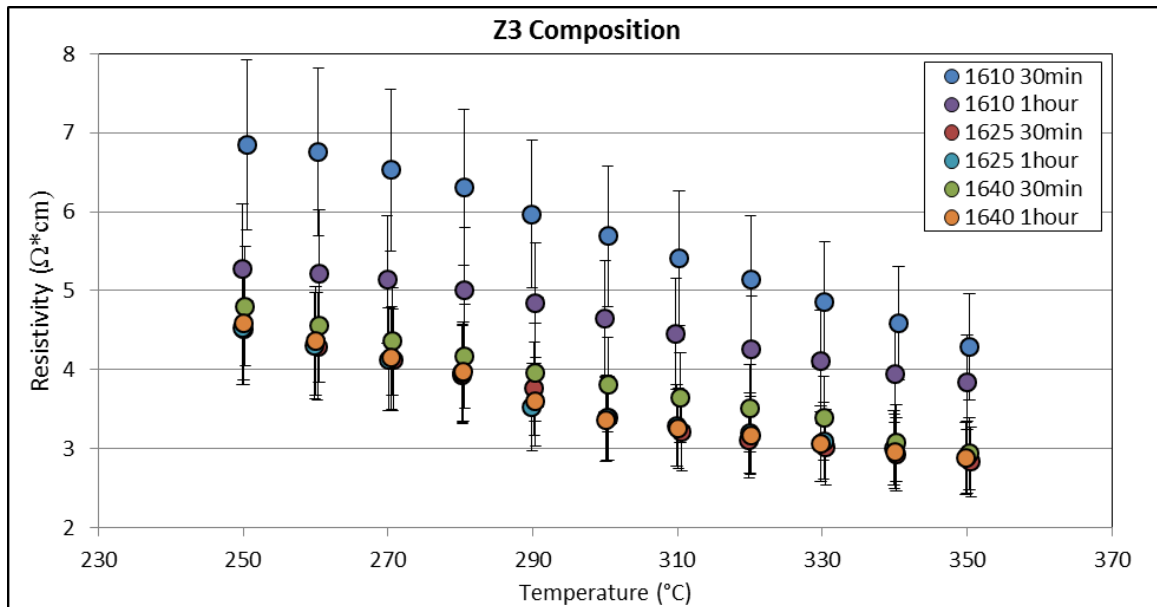


Figure 33. Resistivity vs. temperature for a variety of sintered samples of composition Z3 (0.01 Na/Al excess).

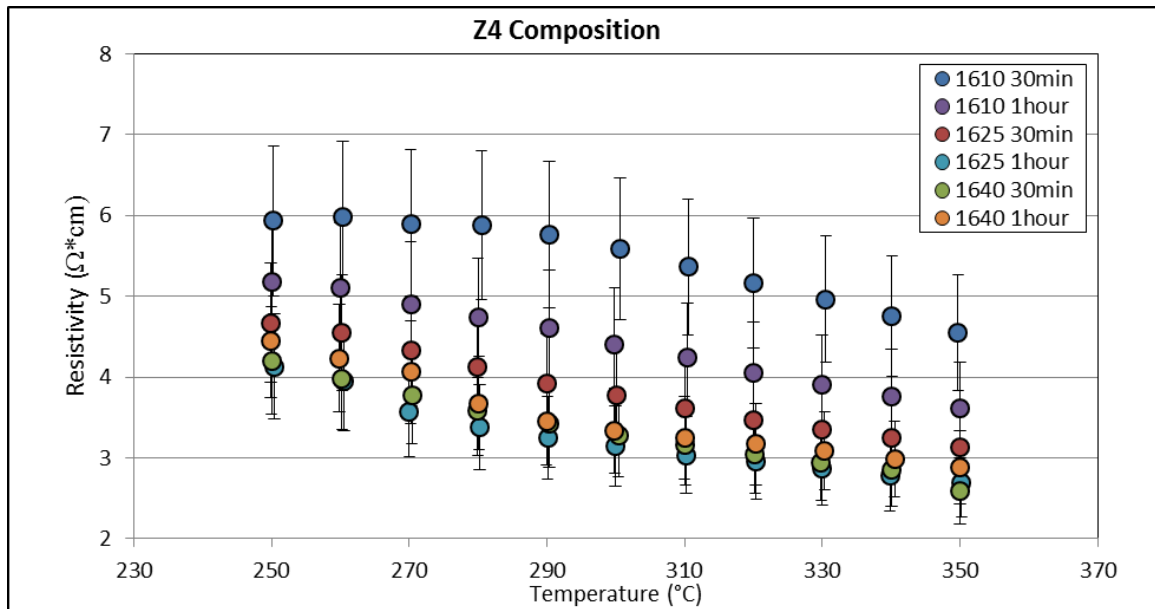


Figure 34. Resistivity vs. temperature for a variety of sintered samples of composition Z4 (0.02 Na/Al excess).

Both figures exhibited trends correlating sample resistivity with temperature. It was observed for both compositions that as the temperature increased, resistivity of the material decreased. This was expected, as ion mobility increases as measurement temperature increases. Additionally, it was observed that for both compositions sample resistivity varied with sintering parameters. Samples sintered at 1610 °C for 30 minutes had the highest resistivity of all samples. Samples sintered to 1610 °C for slightly longer sintering times (1 hour) had the second highest resistivity. For samples sintered from Z3 powder, the remaining samples (1625 °C, 1640 °C for 30 minutes and 1 hour) all had very similar resistivity values. This suggested that after a certain density and grain size were achieved, resistivity remained constant. The same observation applied to samples sintered from Z4 powder. Data collected for 1610 °C 30 minute samples had the highest resistivity of Z4 samples, followed by 1610 °C 1 hour samples. All remaining samples of Z4 composition all had very similar resistivity values (1625 °C, 1640 °C for 30 minutes and 1 hour). This also suggested that at a certain point, resistivity became constant.

The difference in overall resistivity between the two compositions was also evaluated. It was observed that samples of Z3 composition had higher resistivity values overall than Z4 samples when sintered at 1610 °C. However, samples sintered at 1625 °C

and 1640 °C showed very little difference in resistivity between the two compositions. This suggested that sample composition had far less effect on the ionic conductivity of sintered samples than the effects of density and grain size. The comparison of resistivity to other sample properties is considered in the next section.

4. Relationships

a. Effect of Grain Size on Resistivity and Activation Energy

There are several connections that can be made between material properties and ionic conductivity. One such relationship is the correlation between grain size and resistivity. For this study, both Z3 and Z4 sintered samples were examined and their average measured grain sizes were compared to the measured resistivity of the samples.

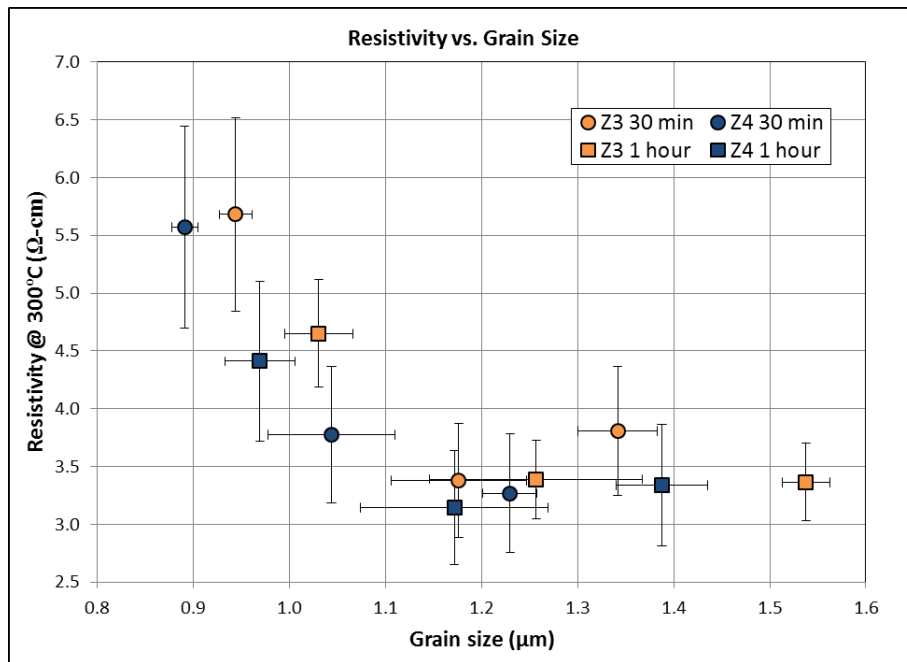


Figure 35. Resistivity vs. grain size for sintered samples.

Figure 35 shows the connection between resistivity and grain size for both Z3 and Z4 samples. It was observed that samples of the Z4 composition (0.06 Na/Al excess) had lower resistivity values than samples of the Z3 composition (0.05 Na/Al) with comparable grain sizes, for samples with smaller grains (<1.1 μm). For samples with larger grains (>1.1 μm), the difference in resistivity was much less and was within the

range of error. This showed that though excess sodium may not have contributed to grain growth as a sintering aid, it did help to improve the electrical performance of the base Na β'' -alumina composition for samples with smaller grain sizes.

In both compositions, an effect of grain size on sample resistivity was observed. There was a linear decrease in resistivity as grain size increased from the smallest grain size (0.891 μm) to about 1.1 μm . At this point, the resistivity of the material leveled off and stayed relatively constant. This indicated that grain size had an effect on the ionic resistivity of the material but not over the entire range of grain size evaluated in this work.

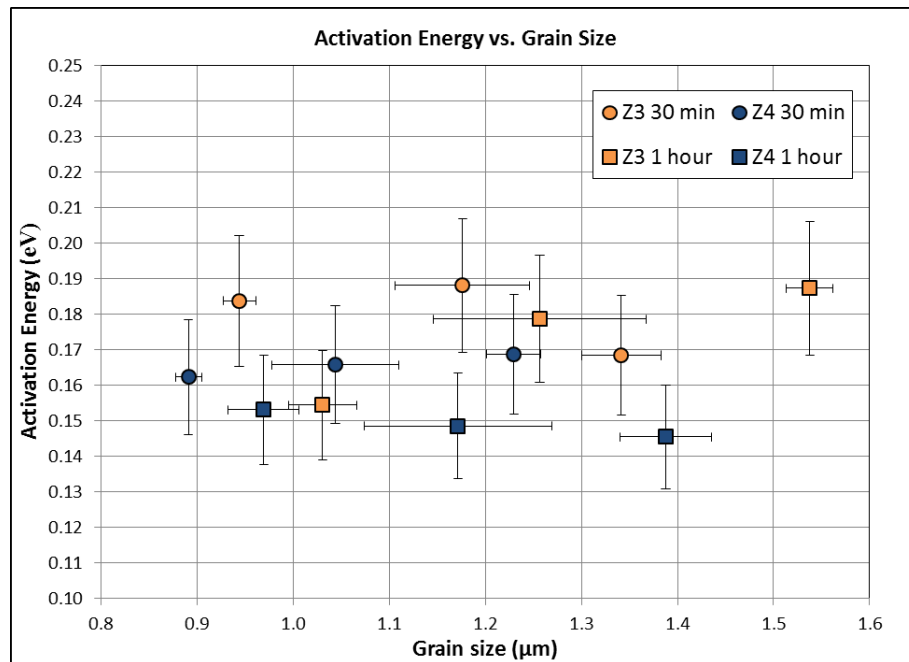


Figure 36. Activation energy vs. grain size for sintered samples.

The correlation of grain size and activation energy for a variety of sintering conditions and compositions is shown in Figure 36. Samples composed of Z3 composition are shown in orange while Z4 samples are shown in blue. Different data shapes illustrate the different sintering times for the samples. It was observed that the samples made from Z3 powders had slightly higher activation energy than those made with Z4 samples; however the results were very similar. In general, it was observed that the grain size had no effect on activation energy.

b. Effect of Density on Resistivity and Activation Energy

Another sample characteristic that can affect ionic resistivity is density. The comparison of sample resistivity to measured density can be seen in Figure 37.

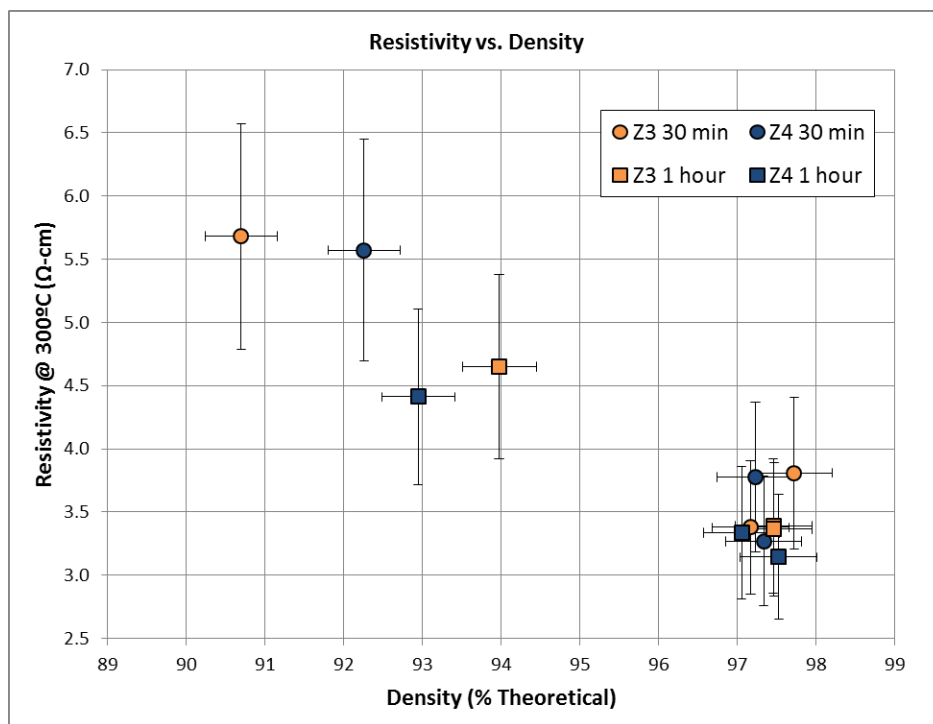


Figure 37. Resistivity vs. density for sintered samples.

It was observed that samples sintered to lower densities (<95% theoretical density) had the highest reported resistivity, as expected. As sample density started to increase, resistivity of the samples decreased. Samples with the highest densities showed the lowest resistivity of all. This trend was more or less linear, at least for the data range examined here. The effect of density on sample activation energy was also examined.

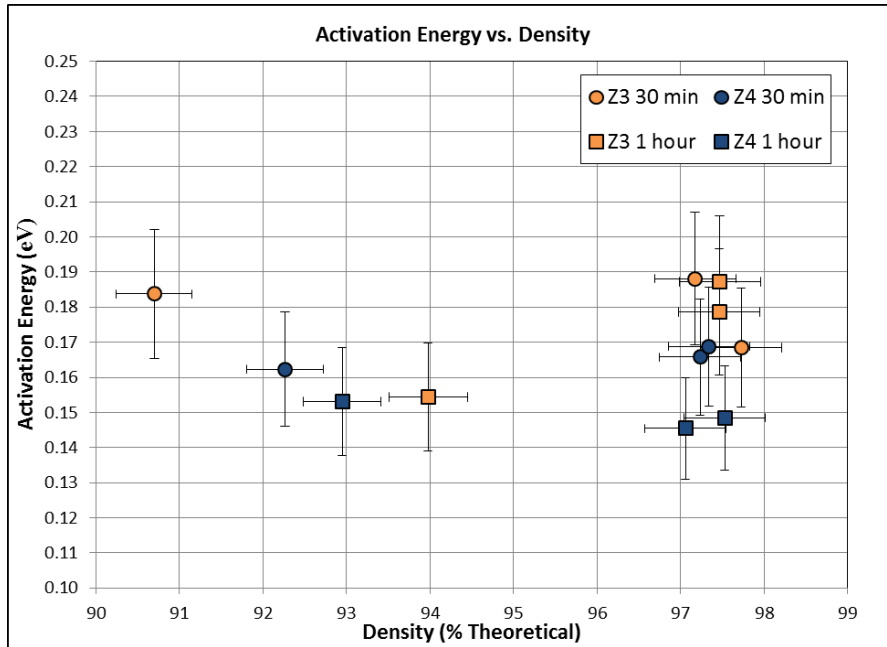


Figure 38. Activation Energy vs. density for sintered samples.

Activation energy data for both compositions sintered at a variety of parameters are all pictured in Figure 38. It was observed that for samples of both compositions, activation energy was constant, regardless of density. The resistivities of the two compositions were also relatively constant. Z3 samples had slightly larger activation energies, but with overlapping error bars with Z4 samples. The average activation energy for these samples was roughly 0.17 eV.

V. SUMMARY AND CONCLUSIONS

A. Effect of Electrode Material on Impedance Measurements

Samples of consistent composition and sintering parameters were measured using impedance spectroscopy. The effects of electrode material and sample thickness on measured impedance were evaluated in this section of work. Four different electrode materials were used during testing: fluxed platinum, unfluxed platinum, gold and carbon.

It was found that sample resistance decreased as sample thickness increased, but that resistivity stayed relatively consistent regardless of sample thickness for all electrode materials. An effect of electrode material on the overall reported resistivity of samples was observed. The effects of contact resistance were quantified to obtain resistivity values representative of only the sample material. Samples measured using fluxed platinum and gold had relatively similar resistivity values, within the margin of error for each sample, although fluxed platinum had slightly higher measured resistivity values than gold. Samples measured using carbon and unfluxed platinum electrodes exhibited overall higher and lower resistivities, respectively. Fluxed platinum, unfluxed platinum and gold electrode data all showed similar average activation energies. Carbon electrode data, however, showed higher activation energy, outside the margin of error. Samples with smaller thickness had a higher degree of uncertainty with respect to resistivity measurements, and that uncertainty decreased with increased sample thickness. Overall, fluxed platinum and gold electrodes produced similar results for activation energy and resistivity which suggests that data collected using either of these materials, would be comparable. Although this study outlined specific steps used to obtain ionic conductivity using impedance spectroscopy, currently there is not one universally accepted standard for these measurements. It is recommended that whenever possible, samples of similar thickness and electrode material should be used. Additionally, it is recommended that samples of greater thickness be used in order to decrease the uncertainty of resistivity measurements. Overall, the use of IS for the measurement of ionic conductivity of these materials is more relative than absolute.

B. Effect of Composition and Sintering on Electrical Properties

The electrical properties of samples sintered to a variety of sintering parameters for two separate compositions were measured. The two compositions used in this work contained slightly different levels of excess sodium from the basic β'' -alumina structure. Several characteristics were evaluated, including density, grain size, chemical composition and diffraction behavior.

X-ray diffraction indicated that the primary phase matched PDF cards for two stabilized β'' -alumina phases: a sodium magnesium aluminum oxide phase ($\text{Na}_2\text{Mg}[\text{Zn}]\text{Al}_{10}\text{O}_{17}$), and a sodium zinc aluminum oxide phase ($\text{Na}_{1.67}\text{Zn}_{0.67}\text{Al}_{10.33}\text{O}_{17}$). In this work, stabilization was performed using the divalent zinc. XRD identification confirmed that the correct phase was synthesized during processing. The presence of a secondary phase was indicated by two small peaks not attributable to the β'' -alumina p. The secondary phase was matched to a sodium aluminate (NaAlO_2) PDF card. Quantifying the amount of this secondary phase by calculating percent peak area proved to be unsatisfactory. The amount of this second phase was very small, less than 5%, and could not be definitively quantified or correlated to sintering parameters or composition.

Two power compositions were synthesized where molar Zn/Al ratios were constant (the same as ideal zinc stabilized phase) and Na/Al ratios varied: 0.01 and 0.02 Na/Al excess from the ideal zinc stabilized phase. ICP analysis was performed on sintered and unsintered samples for both compositions. Zn/Al ratios for both unsintered and sintered Z3 and Z4 compositions were consistent with the ideal composition: Zn/Al = 0.065. However, Na/Al ratios for the two compositions were slightly higher than the target compositions: Z3 and Z4 composition had Na/Al excess of 0.05 and 0.06 respectively. Although there was slightly more excess sodium in the compositions than anticipated, the powders still allowed for the evaluation of small amounts of excess sodium on sintering and ionic resistivity. Additionally, it was observed that Na/Al ratios did not change between unsintered powders and sintered samples, indicating that the precautions used to mitigate sodium loss were effective.

Sample density increased with increased sintering temperature and time, but became constant after a certain temperature. Samples sintered above 1625 °C had very similar densities, greater than 97% theoretical density. Samples with the lowest densities

exhibited the highest measured sample resistivity. As sample density increased, the measured resistivity decreased linearly. Overall, samples densified similarly regardless of composition and no definitive correlation between compositions was observed when resistivity data was related to density.

Microstructures were analyzed to quantify the effect of composition and sintering on grain size. It was observed that samples sintered to higher temperatures and longer sintering time had larger grains. Composition had some effect on overall grain size. Z3 samples had consistently larger grains than Z4 samples, indicating that excess sodium in the composition did not act as a sintering aid. In fact, excess sodium appeared to inhibited grain growth, possibly due to the increased formation of sodium aluminate at the grain boundaries. The effect of microstructure on electrical properties was determined. Samples with small grains had the lowest measured resistivities. Increasing grain size caused a linear decrease in resistivity, until grain size reached roughly 1.1 μm , at which point resistivity became constant. At smaller grain sizes ($<1.1 \mu\text{m}$), it was observed that samples of Z4 composition had smaller resistivities than that of the Z3 compositions. However, once grain size increased, the effect of composition was not a factor, with samples exhibiting very similar resistivities and activation energies.

The major contributions to variations in electrical performance in this work came from density and microstructure. It was not determined that one composition performed better than the other. However, it was observed that excess sodium inhibited grain growth in the material. Therefore, it can be concluded that too much excess sodium in these compositions should be avoided as it does not enhance performance and can aid in the formation of the secondary sodium aluminate phase, which can be detrimental to mechanical performance and stability.

VI. FUTURE WORK

There are two main areas that could be investigated further if future work for this topic were to be performed. The first area would center on the measurements of electrical properties by use of impedance spectroscopy. Although this work has outlined some interesting phenomena associated with impedance spectroscopy testing, it has only really scratched the surface. The use of impedance spectroscopy to quantify electrical performance of conductive materials is still not widely understood. Therefore a detailed study on the use of impedance spectroscopy for quantifying different types of conductive materials could be a very interesting area for future work. Additionally, the evaluation of these same electrode materials and sample thickness at low temperatures would be beneficial.

The second area that could be investigated further is the effect of greater soda excess on the formation of sodium aluminate and the performance of the sintered materials. This study focused on slight amounts of excess sodium in the system, but did not examine the effects of large soda excesses on the phase evolution and electrical properties. This could be another area of interest, particularly if TEM was used to examine the presence of phases at the grain boundaries.

REFERENCES

- 1 J.T. Kummer and Y.F.Y. Yao, "Ion Exchange Properties and Rates of Ionic Diffusion in Beta-Alumina," *J. Inorg. Nucl. Chem.*, **29** [9] 2453–2475 (1967).
- 2 G.E. Youngblood, G.R. Miller, and R.S. Gordon, "Ceramic Microstructures," *J. Am. Ceram. Soc.*, **61** [1-2] 86–87 (1978).
- 3 W. Jakubowski and J. Whitmore, "Analysis of Electrolyte Polarization in Polycrystalline Sodium β -Alumina by a Complex Admittance Method," *J. Am. Ceram. Soc.*, **62** 381 (1979).
- 4 I. Wynn Jones, "Recent Advances in the Development of Sodium-Sulphur Batteries for Load Levelling and Motive Power Applications," *Electrochim. Acta*, **22** [7] 681–688 (1977).
- 5 B.L. Ellis and L.F. Nazar, "Sodium and Sodium-Ion Energy Storage Batteries," *Curr. Opin. Solid State Mater. Sci.*, **16** [4] 168–177 (2012).
- 6 J.D. Hodge, "Alkaline Earth Effects on the Reaction of Sodium with Aluminum Oxide," *J. Electrochem. Soc.*, **133** [4] 833 (1986).
- 7 J.H. Kennedy, "Additives and Resistivities in Beta-Alumina," *Superionic Conduct. Phys. Solids Liq.*, 335–350 (1976).
- 8 J.P. Boilot and J. Théry, "Influence de l'addition d'ions étrangers sur la stabilité relative et la conductivité électrique des phases de type alumine β et β' ," *Mater. Res. Bull.*, **11** [4] 407–413 (1976).
- 9 D. White, S. Chen, H. Harrison, and H. Sato, "Synthesis of Ni-Stabilized β' -Alumina," *Solid State Ionics*, **9-10** 255–258 (1983).
- 10 G. Brown, D. Schwinn, J. Bates, and W. Brundage, "Structures of Four Fast-Ion Conductors by Single-Crystal Neutron-Diffraction Analysis: Zn-Stabilized Na β' -Alumina and Mg-Stabilized Na-, K-, and Ag β' -Aluminas," *Solid State Ionics*, **5** 147–150 (1981).
- 11 A. Imai and M. Harata, "Ionic Conductivity of Impurity-Doped β -Alumina Ceramics," *Jpn. J. Appl. Phys.*, **11** [2] 180 (1971).
- 12 X. Wei, Y. Cao, L. Lu, H. Yang, and X. Shen, "Synthesis and Characterization of Titanium Doped Sodium Beta"-Alumina," *J. Alloys Compd.*, **509** [21] 6222–6226 (2011).
- 13 W.L. Bragg, C. Gottfried, and J. West, "The Structure of Beta Alumina," *Zeitschrift für Krist. - Cryst. Mater.*, **77** [1] 255 (1931).

- 14 C.A. Beevers and M.A.S. Ross, "The Crystal Structure of 'Beta Alumina' $\text{Na}_2\text{O} \cdot 11\text{Al}_2\text{O}_3$," *Zeitschrift für Krist. - Cryst. Mater.*, **97** 59 (1937).
- 15 F. Harbach, "Advantages of Pure Ternary Na- β " - Al_2O_3 Ceramics," *Solid State Ionics*, **5** 279–281 (1981).
- 16 J.L. Sudworth, P. Barrow, W. Dong, B. Dunn, G.C. Farrington, and J.O. Thomas, "Toward Commercialization of the Beta-Alumina Family of Ionic Conductors," *MRS Bull.*, **25** [03] 22–26 (2000).
- 17 M. Bettman and C.R. Peters, "Crystal Structure of $\text{Na}_2\text{O} \cdot \text{MgO} \cdot 5\text{Al}_2\text{O}_3$ [Sodium Oxide-Magnesia-Alumina] with Reference to $\text{Na}_2\text{O} \cdot 5\text{Al}_2\text{O}_3$ and Other Isotypal Compounds," *J. Phys. Chem.*, **73** [6] 1774–1780 (1969).
- 18 G. Yamaguchi and K. Suzuki, "On the Structures of Alkali Polyaluminates," *Bull. Chem. Soc. Jpn.*, **41** [1] 93–99 (1968).
- 19 F. Harbach, "Spinel Block Doping and Conductivity of Sodium Beta"-Alumina Ceramics," *Solid State Ionics*, **13** [1] 53–61 (1984).
- 20 T. Mathews, "Solution Combustion Synthesis of Magnesium Compensated Sodium- β -Aluminas," *Mater. Sci. Eng. B Solid-State Mater. Adv. Technol.*, **78** [1] 39–43 (2000).
- 21 J.H. Kennedy and A.F. Sammells, "Conductivity of Beta-Alumina and Its Dependence on Sodium and Magnesium Content," *J. Electrochem. Soc.*, **119** [12] 1609 (1972).
- 22 R. SeEVERS, J. DeNuzzio, G.C. Farrington, and B. Dunn, "Ion Transfer in Ca^{2+} , Sr^{2+} , Ba^{2+} , and Pb^{2+} Beta" Aluminas," *J. Solid State Chem.*, **50** 146–152 (1983).
- 23 S.J. L. and A.R. Tilley, "The Sodium Sulfur Battery," *Electrochim. Acta*, **32** [5] (1985).
- 24 J.D. Hodge, "Kinetics of the β "-to- β Transformation in the System $\text{Na}_2\text{O}-\text{Al}_2\text{O}_3$," *J. Am. Ceram. Soc.*, **66** [3] 166 (1983).
- 25 H. Engstrom, J. Bates, W. Brundage, and J. Wang, "Ionic Conductivity of Sodium Beta"-Alumina," *Solid State Ionics*, **2** [4] 265–276 (1981).
- 26 J.L. Briant, "Ionic Conductivity in Lithium and Lithium-Sodium Beta Alumina," *J. Electrochem. Soc.*, **128** [9] 1830 (1981).
- 27 N. Weber and A.F. Venero, "Subsolidus Relations in the System NaAlO_2 - MgAl_2O_4 - Al_2O_3 ," *Bull. Am. Ceram. Soc.*, **49** [3] 498 (1970).
- 28 X. Lu, G. Xia, J.P. Lemmon, and Z. Yang, "Advanced Materials for Sodium-Beta Alumina Batteries: Status, Challenges and Perspectives," *J. Power Sources*, **195** [9] 2431–2442 (2010).

- 29 T. Electric and P. Company, "Development of Sodium-Sulfur Batteries," *Int. J.*, **76** 269–276 (2004).
- 30 A. Vanzyl, "Review of the Zebra Battery System Development," *Solid State Ionics*, **86-88** 883–889 (1996).
- 31 C.H. Dustmann, *Ceramic Materials and Components for Engines: Beta Ceramic in Zebra and NAS Batteries*. Wiley VCH, 2001.
- 32 J. Sudworth, "The Sodium/Nickel Chloride (ZEBRA) Battery," *J. Power Sources*, **100** [1-2] 149–163 (2001).
- 33 R.C. Galloway and S. Haslam, "The ZEBRA Electric Vehicle Battery: Power and Energy Improvements," *J. Power Sources*, **80** [1-2] 164–170 (1999).
- 34 J.H. Kennedy and A.F. Sammells, "Galvanic Cells Containing Cathodes of Iron-Doped Beta-Alumina," *J. Electrochem. Soc.*, **121** [1] 1 (1974).
- 35 W. Roth, R. Wong, A. Goldman, E. Canova, Y. Kao, and B. Dunn, "Structure of Additives in β "-Alumina and Zirconia Superionic Conductors," *Solid State Ionics*, **18-19** 1115–1119 (1986).
- 36 M. Wasiucionek, "Electrical Properties of CoO, NiO, CuO and ZnO Doped Beta"-Alumina," *Solid State Ionics*, **7** [4] 283–286 (1982).
- 37 W. Jakubowski and S. Biela, "Electrical Properties of ZnO Stabilized Beta"-Alumina," *Solid State Ionics*, **14** [1] 41–44 (1984).
- 38 W. Jakubowski and D.H. Whitmore, "Analysis of Electrolyte Polarization in Polycrystalline Sodium β " Alumina by a Complex Admittance Method," *J. Am. Ceram. Soc.*, **62** [7-8] 381–385 (1979).
- 39 R.C. DeVries and W.L. Roth, "Critical Evaluation of the Literature Data on Beta Alumina and Related Phases: I, Phase Equilibria and Characterization of Beta Alumina Phases," *J. Am. Ceram. Soc.*, **52** [7] 364–369 (1969).
- 40 D.P. Birnie, "On the Structural Integrity of the Spinel Block in the β "-Alumina Structure," *Acta Crystallogr. Sect. B Struct. Sci.*, **68** [2] 118–122 (2012).
- 41 P. Haycock, "The Structure of Ion Deficient Sodium β " Alumina," *Solid State Ionics*, **80** [1-2] 53–58 (1995).
- 42 J.T. Sampanthar and H.C. Zeng, "Synthesis of Co II Co III Nanocomposites via Sol- Gel Derived γ -Al₂O₃ Matrix," *J. Am. Ceram. Soc.*, **68** [c] 4722–4730 (2001).
- 43 V. Jayaraman, T. Gnanasekaran, and G. Periaswami, "Low-Temperature Synthesis of Beta-Aluminas by a Sol-Gel Technique," *Mater. Lett.*, **30** [2-3] 157–162 (1997).
- 44 T. Takahashi and K. Kuwabara, " β -Al₂O₃ Synthesis From m-Al₂O₃," *J. Appl. Electrochem.*, **10** [3] 291–297 (1980).

- 45 A. Pekarsky and P.S. Nicholson, "The Relative Stability of Spray-Frozen/Freeze-Dried β "-Al₂O₃ Powders," *Mater. Res. Bull.*, **15** [10] 1517–1524 (1980).
- 46 A. Marini, "Hydration and Carbonation of Beta Alumina Powders," *J. Electrochem. Soc.*, **132** [5] 1250 (1985).
- 47 J. Duncan, P. Barrow, A. Van Zyl, and A.I. Kingon, Method of Making Beta'-Alumina; U.S. Pat. 4,732,741, 1988.
- 48 E. Barsoukov and J.R. MacDonald (eds.), *Impedance Spectroscopy*, 2nd ed. Wiley-Interscience, Hoboken, NJ, 2005.
- 49 B. Ulgut, *Electrochemical Impedance Spectroscopy and Its Applications to Battery Analysis*, (2014). Online Webinar: <http://www.gamry.com/application-notes/basics-of-electrochemical-impedance-spectroscopy/>
- 50 P. Fulay, *Electronic, Magnetic, and Optical Materials*, 1st ed. CRC Press, Boca Raton, FL, 2010.
- 51 D.P. Almond, A.R. West, and R.J. Grant, "Temperature Dependence of the A.C. Conductivity of Na β -Alumina," *Solid State Commun.*, **44** [8] 1277–1280 (1982).
- 52 J.H. Kim, E.C. Shin, D.C. Cho, S. Kim, S. Lim, K. Yang, J. Beum, J. Kim, *et al.*, "Electrical Characterization of Polycrystalline Sodium β "- Alumina: Revisited and Resolved," *Solid State Ionics*, **264** 22–35 (2014).

APPENDIX

A. Batch Sheets

Gamma alumina (Sudworth Step #1) Batch		Body Formulation			Ana Fredell
5 kg					wt% (dwb) wt% (dwb) (Normalize ratio d)
A. Non Combustibles			M.W. (g/mol)		
1	γ-Alumina	Al ₂ O ₃	59.99	3.329 kg	66.6%
		S.S.A.: 34.01 m ² /g Density: 2.95 g/cc LOI: 1.17%			
2	Sodium Carbonate Monohydrate	Na ₂ (CO ₃)·H ₂ O	124.00	686.39 g	13.7%
		S.S.A.: - m ² /g Density: 2.54 g/cc LOI: 50.00%			
3	Zinc Acetate DiHydrate	Zn(C ₂ H ₃ O ₂) ₂ * 2H ₂ O	219.54	984.99 g	19.7%
		S.S.A.: - m ² /g Density: - g/cc LOI: 65.90%			
Total:				5.000 kg	100.0%
B. Combustibles					
4	Darvan 811	Na-PAA	8900.00	92.14 g	0.79%
		Effective Solids: 43.00% (wt) Degree Dispersion: 0.35 mg/m ²			
C. Water / pH Adjustment					
7	Deionized Water		18.02	3.093 kg	
		Effective Solids: 0.00% (wt)			
	Average Solid Phase	2.95 g/cc			
	Specific Gravity:	1.69 g/cc			
	Solids Loading (wt%)	61.6%			
	(vol%)	35.00% 35.00%			
	Volume of Slurry:	4.85 L			
		COMPOSITION TARGETS			
		Al ₂ O ₃	76.953 mol%	82.890 wt%	
		101.96 g/mol			
		Na ₂ O	13.207 mol%	8.647 wt%	
		61.98 g/mol			
		ZnO	9.841 mol%	8.463 wt%	
		81.41 g/mol			

Figure 39. Batch sheet for Z3 composition.

Gamma alumina (Sudworth Step #1)				Body Formulation		Ana Fredell
Batch		5 kg				
				wt%	wt% (dwb)	
				(dwb)	(Normalize	
				ratio	d)	
A. Non Combustibles				M.W. (g/mol)		
1	γ -Alumina	Al_2O_3	59.99	3.297 kg	65.9%	
	S.S.A.:	34.01	m^2/g			
	Density:	2.95	g/cc			
	LOI:	1.17%				
Sodium Carbonate						
2	Monohydrate	$\text{Na}_2(\text{CO}_3)\cdot\text{H}_2\text{O}$	124.00	718.26 g	14.4%	
	S.S.A.:	-	m^2/g			
	Density:	2.54	g/cc			
	LOI:	50.00%				
3	Zinc Acetate DiHydrate	$\text{Zn}(\text{C}_2\text{H}_3\text{O}_2)_2 \cdot 2\text{H}_2\text{O}$	219.54	984.48 g	19.7%	
	S.S.A.:	-	m^2/g			
	Density:	-	g/cc			
	LOI:	65.90%				
				Total:	5.000 kg	100.0%
B. Combustibles						
4	Darvan 811	Na-PAA	8900.00	91.28 g	0.78%	
	Effective Solids:	43.00%	(wt)			
	Degree Dispersion:	0.35	mg/m^2			
C. Water / pH Adjustment						
7	Deionized Water		18.02	3.094 kg		
	Effective Solids:	0.00%	(wt)			
	Average Solid Phase	2.95	g/cc			
	Specific Gravity:	1.69	g/cc			
	Solids Loading (wt%)	61.6%				
	(vol%)	35.00%	35.00%			
	Volume of Slurry:	4.85	L			
				COMPOSITION TARGETS		
	Al_2O_3	76.317	mol%	82.425	wt%	
		101.96	g/mol			
	Na_2O	13.836	mol%	9.084	wt%	
		61.98	g/mol			
	ZnO	9.847	mol%	8.491	wt%	
		81.41	g/mol			

Figure 40. Batch sheet for Z4 composition.

B. TGA Results

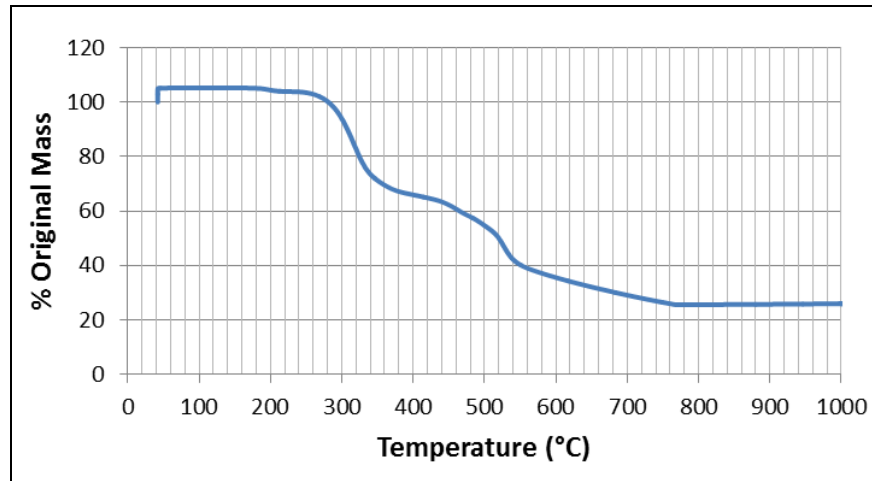


Figure 41. TGA data for uncalcined powder of Z3 composition.

C. MatLab Code

MatLab code written by Bu Wang (Post Doctoral Researcher, Alfred University 2014).

```
% Impedance compensation script
% 04/10/2014 Bu Wang
%
% 1. Raw data files should be in a folder named "data";
% 2. Double check Rp, Cp, Rs and Ls below;
% 3. Run script; will process every files in "data";
% 4. Compensated data files will be in the "compensated" folder under
%    "data". File names start with "c-", followed by the original name.
%
% * files other than impedance data in the "data" folder will cause error
% ** last three columns are not modified

clear,clc;

% compensation with open circuit Rp and Cp in parallel, close circuit Rs
% and Ls in series:

Rp=1e8;
Cp=6e-12;

Rs=0.0028128;
Ls=2.528e-8;

cd ./data;
flist=dir;
mkdir compensated;
```

```

for k=1:size(flist,1)
    fname=flist(k).name;
    [stat ftype]=fileattrib(fname);
    if fname(1)~='.' & ftype.hidden~=1 & ftype.directory~=1

        fin=fopen(fname);
        fgetl(fin);
        fgetl(fin);
        fgetl(fin);
        fgetl(fin);
        line5=fgetl(fin);
        line6=fgetl(fin);
        datapoints=textscan(line6,'Data Points:%u');
        line7=fgetl(fin);
        frewind(fin);
        data=textscan(fin,[ repmat(['%f'],1,8)],'HeaderLines',7);
        fclose(fin);

        data=cell2mat(data);
        if datapoints{1}~=size(data,1)
            fprintf('NO. of data points mismatch!\n')
        end
        f=data(:,1);
        Zm=data(:,2)+1i*data(:,3);
        Zp=1./(1/Rp+(2i*pi*f*Cp));
        Zs=Rs+1i*2*pi*f*Ls;
        Z=Zp.*(Zm-Zs)./(Zp-(Zm-Zs));

        data(:,2)=real(Z);
        data(:,3)=imag(Z);
        data(:,4)=abs(Z);
        data(:,5)=180*(angle(Z))/pi;

        fout=fopen(['compensated/c-',fname],'w');
        fprintf(fout,'NYSCC @ Alfred University\n');
        fprintf(fout,'Contact Bu Wang for the compensation script\n');
        fprintf(fout,'Raw data from LabVIEW Program Z-DAQ\n');
        fprintf(fout,'Compensation:
Rp=%3.1e,Cp=%3.1e,Rs=%5.3f,Ls=%4.2e\n',Rp,Cp,Rs,Ls);
        fprintf(fout,[line5,'\n']);
        fprintf(fout,'Data Points: \t%3u',size(data,1));
        fprintf(fout,'\n');
        fprintf(fout,[line7,'\n']);
        fprintf(fout,[ repmat(['%8.3E\t'],1,8),'\n'],data');
        fclose(fout);

    end
end

fclose all;

```